Journal of Asian Earth Sciences 113 (2015) 218–237

Contents lists available at ScienceDirect

Journal of Asian Earth Sciences

journal homepage: www.elsevier.com/locate/jseaes

Petrology and geochemistry of late Carboniferous hornblende gabbro from the Awulale Mountains, western Tianshan (NW China): Implication for an arc–nascent back-arc environment

Shuang Yan [a,b], Qiang Shan [a,*], He-Cai Niu [a], Wu-Bin Yang [a], Ning-Bo Li [a,b], Ling-Jun Zeng [a,b], Yu-Hang Jiang [a,b]

[a] CAS Key Laboratory of Mineralogy and Metallogeny, Guangzhou Institute of Geochemistry, Chinese Academy of Sciences, Guangzhou 510640, China
[b] University of Chinese Academy of Sciences, Beijing 100049, China

ARTICLE INFO

Article history:
Received 15 September 2014
Received in revised form 11 January 2015
Accepted 19 January 2015
Available online 28 January 2015

Keywords:
Hornblende gabbro
Awulale Mountains
South Tianshan Ocean subduction
Nascent back-arc environment
CAOB

ABSTRACT

The Awulale Mountains, the conjunction point of the Tarim Plate, Junggar Plate and Yili-Central Tianshan Block, are the crucial place to decipher the tectonic evolution of the western Tianshan. We report results of petrologic, whole-rock geochemical, Sr–Nd isotopic data and in-situ zircon U–Pb and Hf isotopes for the Wuling (poikilitic) hornblende gabbro from the Awulale Mountains, western Tianshan. Two stage crystallization processes are applied to interpret its mineral composition. Zircon U–Pb ages indicate that the Wuling hornblende gabbro was emplaced during the late Carboniferous (313 Ma ± 3 Ma). The Wuling hornblende gabbro is characterized by tholeiitic affinity with low $^{87}Sr/^{86}Sr$ ratios, positive $\varepsilon_{Nd}(t)$ and zircon $\varepsilon_{Hf}(t)$ values, resembling its coeval mafic rocks in the Awulale Mountains. They are enriched in large ion lithophile elements (LILEs) and depleted in high field strength elements (HFSEs), indicating a subduction-related setting for their generation and their mantle source were mainly fluxed by fluids released by the down-going slab. The flat REE and depleted Sr–Nd–Hf isotopic signatures imply a shallow and heterogeneous mantle source with the involvement of a deep MORB-like component. We propose that an arc–nascent back-arc system had been developed between the Nalati Mountains and the Awulale Mountains during the late Carboniferous, where the magma derived from decompression melting of MORB-like mantle caused by the slab roll-back and flux-induced melting of mantle wedge were both contributed to their generation. The arc-type features of them were inherited from the strong subduction input at the initiation of back-arc rifting. However, the back-arc rifting ceased at the end of late Carboniferous because of the compressional stress from the collision between the Tarim Plate and the Yili-Central Tianshan Block.

1. Introduction

The east–west-trending Awulale Mountains are located in the southwestern Central Asia Orogenic Belt, lying in the conjunction of Tarim Plate, Junggar Plate and Yili-Central Tianshan Block (YCTB). It is an important orogenic belt as well as a significant polymetallic metallogenic belt, containing numerous Late Paleozoic volcanic and intrusive rocks and associated Fe–Cu deposits (Hong et al., 2003; Xiao and Kusky, 2009; Zhang et al., 2014). However, the tectonic evolution and nature of this belt are still in controversy. Contrasting models have been proposed for Late Paleozoic tectonic evolution of the Awulale Mountains. Some researchers suggest the Paleozoic ocean basin in the Tianshan region had closed during the early Carboniferous and a post-orogenic rift setting accompanied by extensive continental rift-type volcanism was developed in the YCTB (Xia et al., 2004a,b, 2008). The other researchers suggest a continental arc setting in the YCTB during the Late Paleozoic and the related subduction lasted until Late Permian–Triassic (Zhang et al., 2007a,b; Xiao et al., 2010, 2013). During the Late Paleozoic, the Yili Block over-rode the subducting slabs of the South Tianshan Ocean from the south and the North Tianshan Ocean from the north (Wang et al., 2008; Gao et al., 2009; Xiao et al., 2013). Therefore, there is a debate on the polarity of the subduction that the Awulale orogen was mainly subjected to. It is generally recognized that the tectonic setting of the Awulale Mountains in Late Paleozoic was mainly controlled by northward subduction of the Southern Tianshan Ocean (e.g., Gao et al., 2009; Zhu et al., 2009; Yang et al., 2012, 2014a; Xiao et al., 2013; Li et al., 2015a). Thus, the key issue is on the timing of final closure

* Corresponding author. Fax: +86 20 85290130.
E-mail address: qshan@gig.ac.cn (Q. Shan).

http://dx.doi.org/10.1016/j.jseaes.2015.01.016
1367-9120/

of the South Tianshan Ocean or the collision between Tarim plate and the YCTP. The collision is thought to have occurred either during Devonian–Carboniferous according to the age of associated ophiolitic mélanges (Charvet et al., 2007; Wang et al., 2011), or during the Carboniferous–Permian period based on the occurrence of syn- and/or post-collision-related rocks (Gao et al., 2009; Long et al., 2011; Yang et al., 2012) and the metamorphic zircon ages of eclogite (Hegner et al., 2010; Li et al., 2010b; Su et al., 2010; Wang et al., 2010, 2011), or even during the Permian–Triassic period because of the tectonic reconstructions (Xiao et al., 2010, 2013). Fortunately, we can utilize the petrogenetic processes and geochemical signature of typical rocks as arbiters to discriminate and further constrain these competing models.

Hornblende-bearing gabbros are typical of subduction-related magmatic rocks and have been considered to represent magmatic differentiation process in arc magmas (Arculus and Wills, 1980; Beard, 1986; Debari, 1994; Hickeyvargas et al., 1995; Mandal et al., 2012). The presence of abundant hornblende in the subduction-related gabbroic rocks has been considered either as an early stage mineral crystallized directly from the water-rich basaltic magma (Conrad and Kay, 1984; Beard and Borgia, 1989; Wan et al., 2013) or as a product of reaction between early stage minerals (olivine, pyroxene and plagioclase) and water-rich evolved melt (Dong et al., 1997; Prouteau et al., 2001; Costa et al., 2002; Yan and Niu, 2014). Petrographically, the former type of hornblende usually occurs as smaller crystals in gabbroic rocks and anorthite exists as the most extreme end product in the late crystallization stage (e.g., Ulmer et al., 1983; Sisson et al., 1996; Wan et al., 2013) as a high water content in a basaltic magma often suppresses the crystallization of plagioclase (Sisson and Grove, 1993). Whereas, the later type usually occurs as poikilitic crystals enclosing earlier-formed plagioclase grains and showing reaction relation with them (e.g., Smith et al., 1983; Ulmer et al., 1983; Dong et al., 1997; Costa et al., 2002; Bonev and Stampfli, 2009; Mandal et al., 2012).

Our studied mafic intrusion outcrops in the Wuling area of the Awulale Mountains and consists of undeformed gabbro and minor diorite. In this study, we focus on the petrogenesis of the Wuling gabbroic rock and identify it as (poikilitic) hornblende gabbro based on the petrographic observation. A systematical investigation was carried on petrography, mineral microanalyses, whole-rock geochemistry and Sr–Nd isotopes, and zircon U–Pb geochronology and in-situ Hf isotope for the Wuling hornblende gabbro, in order to constrain its petrogenesis and source nature, and to reveal the geodynamic setting.

2. Geological background and petrography

2.1. Regional geology

The Tianshan orogenic belt extends west–east for ca. 2500 km along the southwestern margin of the Central Asian Orogenic Belt (CAOB, also known as the Central Asian Orogenic System or CAOS) (Fig. 1a), a typical accretionary orogenic belt formed by multistage accretionary collage of various micro-continents, continental fragments, and arc complexes from Precambrian to Mesozoic (Sengor et al., 1993; Jahn, 2004; Xiao et al., 2004, 2008). Western Tianshan (Fig. 1b), the western part of Chinese Tianshan, is sandwiched between the Junggar plate to the north and the Tarim plate to the south, and subdivided into three parts, i.e., the North Tianshan, the Central Tianshan (or Yili-Central Tianshan) and the South Tianshan (Windley et al., 1990; Allen et al., 1993; Gao et al., 1998, 2009; Wang et al., 2008, 2011; Han et al., 2010, 2011). The Yili block is an elongated wedge-shape terrain within the Central Tianshan, tapering to a point where Keguqing–Boluokrlu Mountains and Haerke–Nalati Mountains converge (Fig. 1b).

The Awulale Mountains, lying in the northeastern part of the Yili Block and connecting Tarim, Junggar and Yili Block (Fig. 1c), has a Mesoproterozoic metamorphic crystalline basement that is predominately comprised of marble, biotite–plagioclase gneiss and hornblende-two-feldspar gneiss (Feng et al., 2010), and is covered by a series of carbonate-volcanic rocks, marine volcanic and volcaniclastic rocks, terrigenous clastic-carbonate rocks and terrigenous clastic rocks produced during the period from the Silurian to the Jurassic (Feng et al., 2010; Hu et al., 2000; Li et al., 2009a, 2009b; Liu et al., 2014; Luan et al., 2008; Wang et al., 2014a, 2014b). In addition, the Awulale Mountains are also a polymetallic metallogenic belt, named as the Awulale Fe–Cu Metallogenetic Belt (AMB) (Zhang et al., 2012, 2014). The Fe deposits are mainly distributed in the eastern part of the AMB while the Cu deposits in the western part. In the eastern part of the AMB, the Precambrian basement is unconformably overlain by the Dahalajunshan Formation, which hosts the majority of the magnetite orebodies in this region. Locally, Permian to Triassic continental sedimentary rocks, consisting of conglomerate, sandstone, mudstone, and shale, unconformably overlie the Carboniferous volcanic and volcaniclastic strata. Abundant Permian dikes like porphyritic diorite, diabase, porphyritic diabase, and lamprophyre, etc., occur in the region, some of which crosscut the volcanic strata, the alteration zones, and the iron orebodies (Jiang et al., 2014).

2.2. Local geology and petrography

The Wuling iron ore deposit, which was discovered recently, is situated in the eastern part of the AMB (Fig. 1c). Strata outcroping in the studied area (Fig. 2) contain the Quaternary sediments and the Lower Carboniferous Dahalajunshan Formation. The Dahalajunshan Formation is composed of volcanoclastic rocks, acidic-basic lavas and tuffs and carbonate rocks. Two sub-Formation of the Dahalajunshan Formation are exposed in the studied area. The first sub-formation (C_1d_a) crops out in the northwestern part of the studied area, composed of gray thick-bedded acidic-neutral volcanic rock, limestone, siliceous rock and basalt porphyrite. The second one (C_1d_b) is exposed in the southeastern part of the studied area, consisting of andesitic lithic-crystal tuff, sodium lithic tuff and fine-crystal limestone. Moyite, granite porphyry, diorite, gabbro intrude the Lower Carboniferous volcanic rocks of Dahalajunshan Formation (refer to the Wuling Iron ore deposit work report).

The Wuling mafic intrusion is a ca. 20 km^2 scale apophysis, located in the north of the Wuling iron ore deposit, displaying a close relationship with the iron orebodies. The Wuling intrusion consists of undeformed gabbro and minor diorite. In this study, we focus on the gabbroic rocks of the intrusion and name it as (poikilitic) hornblende gabbro based on detailed petrographical observation. The Wuling hornblende gabbro mainly exhibits massive structures and evident texture zoning with three kinds of granular textures in the field, i.e., coarse-grain, coarse- to medium-grain, and fine-grain (Fig. 3a) from the core to the rim of the pluton. The hornblende gabbro contains plagioclase (~40–45 vol.%), hornblende (~35–45 vol.%), clinopyroxene (~5–10 vol.%), Fe-oxides (magnetite and ilmenite) (~5–10 vol.%) and epidote (~2–5 vol.%) with a few accessory minerals like apatite and zircon. Some samples have experienced slight alteration, for example, sericitization occurs in plagioclase grains, and chloritization and actinolitization are present in some hornblende grains. Plagioclase crystals are variable in texture from euhedral, subhedral to anhedral. The anhedral ones, actually relic grains of plagioclase, are poikilitically enclosed within and even absorbed by giant hornblende crystal (Fig. 3d and e). At some place, the plagioclase exhibits corrosion texture and partly included by the hornblende (Fig. 3b). At other place,

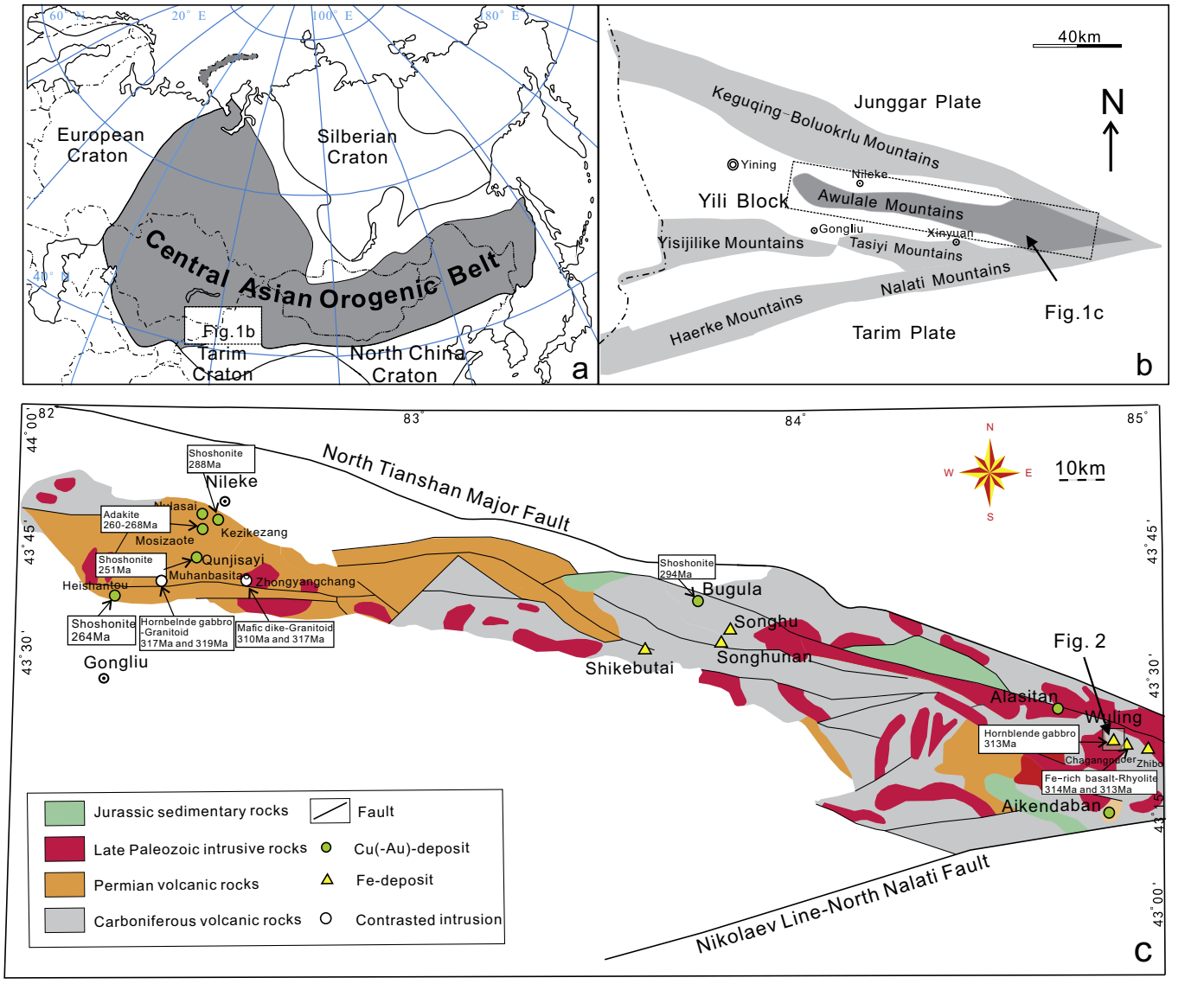

Fig. 1. (a) Tectonic sketch map of the Central Asia Orogenic Belt and the location of the Tianshan orogen (Sengor et al., 1993; Xiao et al., 2010); (b) simplified tectonic-geological sketch map of the Awulale Mountains (modified from Niu et al. (2012)); (c) geological map of the Awulale metallogenic belt (modified from Zhao et al. (2000) and Yang et al. (2012)).

the euhedral plagioclase grains cut the hornblende grains (Fig. 3c). Hornblende grains in Wuling gabbro are subhedral and anhedral, exhibiting pleochroism from green to greenish brown in polarized light. These hornblende grains are thought to be the product due to reaction of early stage minerals (pyroxene and plagioclase) and water-rich evolved melt. Pyroxene crystal is less abundant and anhedral, mostly embedded in hornblende crystal (Fig. 3d and e). At some places, pyroxene is only partly altered to hornblende along the crystal margin. At other places, pyroxenes are totally replaced by hornblende. Although there are no pyroxene relics, their natures imply that they are the alteration products. The Fe-oxides mainly are magnetite and ilmenite. Intergrowth of magnetite and ilmenite grains is common. Some Fe-oxides are hosted by hornblende grains without obvious reaction rim between each other (Fig. 3d and e) and exhibit exsolution textures, while others are intergranular. On the basis of textural relationships, the mineral crystallization sequence may be as follows: (1) early-stage minerals: clinopyroxene + subhedral and anhedral plagioclase + subhedral magnetite; (2) late-stage minerals: hornblende + euhedral plagioclase + magnetite.

3. Analytical methods

3.1. Electron microprobe analysis

Mineralogical investigation on sample 13WL was carried out by an electron probe micro analyzers (JEOL EPMA JXA–8800R) equipped with five wave-length dispersive spectrometers (WDS) at the Instrumental Analysis and Research Center, Sun Yat-Sen University. Secondary and backscattered electron images were used to guide the analysis on target positions of minerals. An 1-μm defocused beam was operated for analysis at an acceleration voltage of 12 kV with a beam current of 6 nA. The measured X-ray intensities were corrected by ZAF method using the standard calibration of synthetic chemical-known standard minerals with various diffracting crystals, as follows: wollastonite for Si with TAP crystal, corundum for Al (TAP), Cr-oxide for Cr with PET crystal, haematite for Fe with LiF crystal, Mn-oxide for Mn (PET), periclase for Mg (TAP), Ni-oxide for Ni (LiF), wollastonite for Ca (PETH), albite for Na (TAP), orthoclase for K (PET), apatite for P (PET) and fluorite for F (TAP). The X-ray peak counting times for the upper and lower

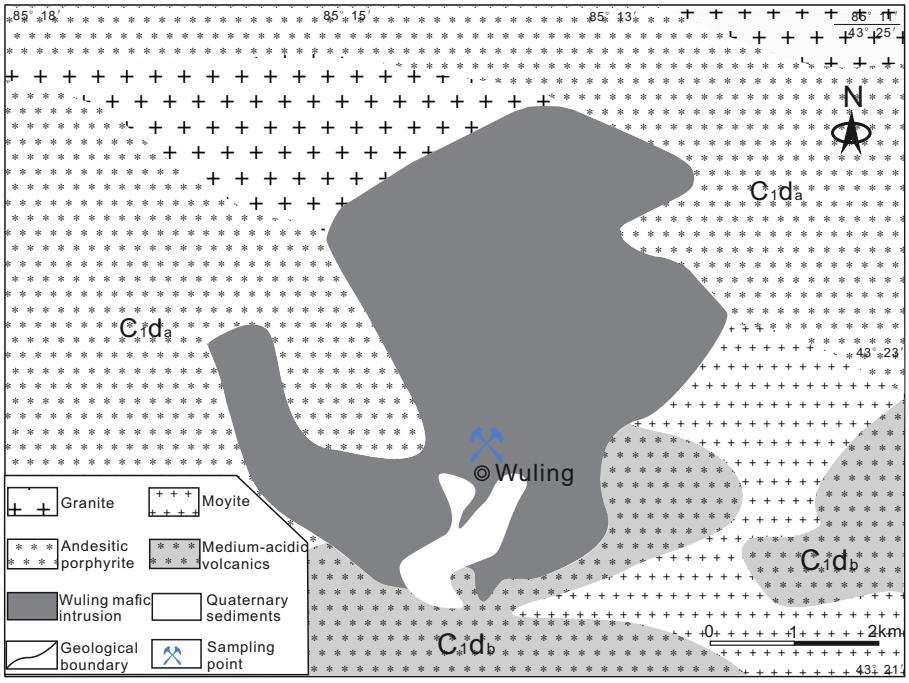

Fig. 2. Geological map of the Wuling area and the sampling point (modified from 1:20,000 geological map of Wuling region, Hejing County, Xinjiang).

baselines of each element were 10 s and 5 s, respectively. Standards run as unknowns yielded relative standard deviations of <2% for F and P, <1% for Si, Na and K, and <0.5% for other elements. Detection limits were <0.5 wt.% for F and P and <0.5 wt.% to 600 ppm for all other elements.

3.2. Zircon U–Pb dating and Hf isotope

Zircon grains were firstly separated through powdering fresh gabbro samples to about 80 mesh, desliming in water, followed by density separation, magnetic separation and handpicking, then mounted in epoxy and polished to nearly a half section to expose internal structures. Cathodoluminescent (CL) and optical microscopy images of zircon grains were obtained in order to ensure that the least fractured, inclusion-free zones in zircon were analyzed. Zircon U–Pb dating of Wuling gabbro was undertaken by using the laser ablation inductively coupled plasma spectrometry (LA–ICP–MS), at the State Key Laboratory of Isotope Geochemistry, Guangzhou Institute of Geochemistry, Chinese Academy of Sciences (GIGCAS). NIST SRM 610 glass (Pearce et al., 1997), Temora zircon standards (Black et al., 2003) and Plesovice zircon standards (Slama et al., 2008) are used as external standards. All analyses were carried out at an energy of 80 mJ, with a beam diameter of 31 μm and a repetition rate of 10 Hz. Integration of background and analytical signals, and time-drift correction and quantitative calibration for trace elements, were undertaken by using the ICPMADataCal 7.7 (Liu et al., 2010a,b; Li et al., 2012). Concordia diagrams and weighted mean calculations were made using Isoplot 4.11 (Ludwig, 2008). Results are presented in Table 2.

Zircon Hf isotope measurements were carried out on a resolution M-50 type 193 nm excimer laser ablation system of Resonetics, attached to Neptune Plus multi-collector ICP-MS, at the Sate Key Laboratory of Isotope Geochemistry, GIGCAS. The Hf analyses were done at the same spot of zircon U–Pb analyses using a spot size of 45 μm, an 8 Hz pulse rate and a laser power of 80 mJ/pulse. Every 5 analyses were followed by standards zircon Penglai (Li et al., 2010a). The analytical protocol used was similar to that outlined in Wu et al. (2006). The isobaric interference of ^{176}Lu and ^{176}Yb on ^{176}Hf was corrected by using the recommended $^{176}Lu/^{175}Lu$ ratio of 0.02669 (Debievre and Taylor, 1993) to calculate $^{176}Lu/^{177}Hf$ and the recommended $^{176}Yb/^{172}Yb$ ratio of 0.5886 (Chu et al., 2002) to calculate $^{176}Hf/^{177}Hf$ ratios. Results are presented in Table 3.

3.3. Whole-rock geochemical analyses

Whole-rock samples from the Wuling gabbro were examined by optical microscopy. Only unaltered or least-altered samples were selected for geochemical analyses. The major and trace elements are analyzed at the State Key Laboratory of Isotope Geochemistry, GIGCAS. Major elements were determined using the standard X-ray fluorescence (XRF, Rigaku RIX 2100) method (Li et al., 2005), with analytical precision better than 4%. Trace elements were analyzed by inductively coupled plasma mass spectrometry (ICP-MS), using a Perkin–Elmer Sciex ELAN 6000 instrument. Analytical precision for most elements is better than 2–5% (Li, 1997). Major and trace elements results are listed in Table 1.

For Sr–Nd isotope determination, sample powders were first dissolved in Teflon capsules with $HF + HNO_3$ acid. Secondly, Sr and REE were separated by using cation columns, and then Nd fractions were further separated by using HDEHP-coated Kef columns. Sr and Nd isotopic compositions were analyzed on the Micro-mass Isoprobe multi-collector mass spectrometer at GIGCAS, following procedures similar to those of Wei et al. (2002) and Liang et al. (2003). Measured $^{87}Sr/^{86}Sr$ and $^{143}Nd/^{144}Nd$ ratios were normalized to $^{86}Sr/^{88}Sr = 0.1194$ and $^{146}Nd/^{144}Nd = 0.7219$, respectively. The $^{87}Sr/^{86}Sr$ ratio of the Standard NBS SRM 987 and the $^{143}Nd/^{144}Nd$ ratio of the Standard Shin Etsu JNdi-1 determined during this study were 0.71025 and 0.512115, respectively. Results are presented in Table 4.

4. Analysis results

4.1. Mineral chemical data

Major oxide compositions of plagioclase, hornblende and pyroxene are listed in the online Supplementary material

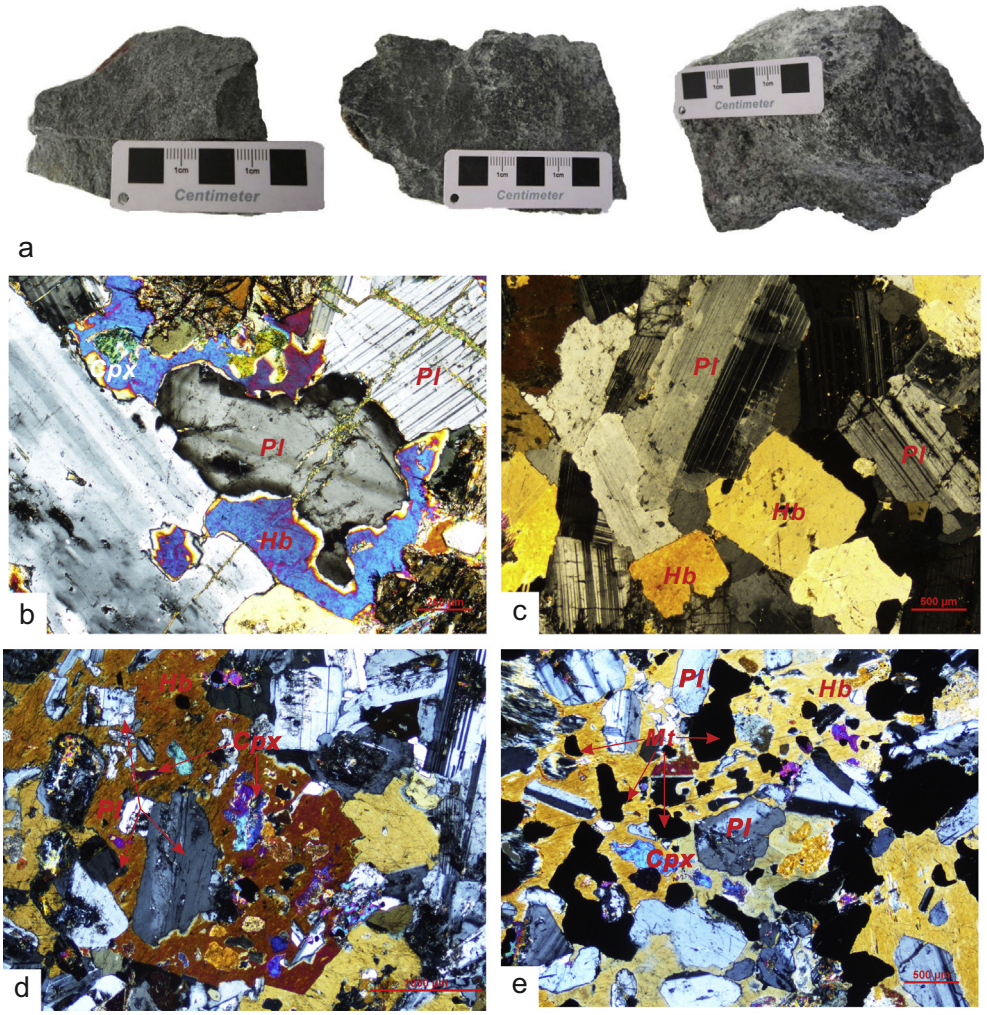

Fig. 3. Hand specimens and Petrography observation (cross-polarized light) of the Wuling gabbro: (a) fine-grained gabbro, medium-grained gabbro and corase-grained gabbro from left to right; (b) corrosion of plagioclase by the melt; (c) plagioclase grain cuts hornblende grain; (d) xenomorphic plagioclase and clinopyxene cystals enclosed within hornblende grain; (e) Fe-oxides enclosed within hornblende grain. Abbreviations here: Hb: hornblende; Cpx: clinopyxene; Pl: plagioclase; Fe: Fe-oxide.

(Table S1). The composition of the plagioclase (12 analyses) is predominately anorthite with An ranging from 91 to 96 with one analyses spot of albite composition (An = 2.3). The anorthite has CaO contents ranging from 16.3 wt.% to 18.8 wt.% with modest amounts of FeO (<0.4 wt.%) and K_2O (0.03–0.13 wt.%). Pyroxene (10 analyses) compositions fall within the diopside field of the pyroxene quadrilateral. They have TiO_2 contents varying from 0.05 wt.% to 0.53 wt.% and Cr_2O_3 contents ranging from below detection limit to 0.06 wt.%. The composition of amphiboles (4 analyses) are magnesiohornblende with MgO contents ranging from 13.8 wt.% to 14.2 wt.% and FeO contents from 12.1 wt.% to 12.7 wt.%. They have narrow but high Mg# values from 66.4 to 67.7.

4.2. Zircon U–Pb geochronology, Ti-in-zircon thermometer and zircon Hf isotope

Zircon crystals from the Wuling gabbro are transparent, light olive brown, showing two types of crystal forms, namely prismatic shape and dipyramidal shape (Fig. 4). The former are relatively large with length ranging from 200 to 400 μm and width from 100 to 150 μm. While for the later, they are 100- to 200-μm-long and 80- to 100-μm-wide. Most of the zircon grains occur as euhedral, prismatic minerals, with regular oscillatory magmatic zonings and without inherited cores (Fig. 4). Th and U contents are 40–320 ppm and 58–310 ppm, respectively and their Th/U ratios (ranging from 0.47 to 1.03) (Table 2) are relatively high and consistent with those of the magmatic zircon (>0.4) (e.g., Belousova et al., 2002; Yang et al., 2014b).

Thirty-two U–Pb analyses of zircon grains are well concordant with all concordia degrees above 90%. The $^{206}Pb/^{238}U$ ages range from 299 Ma to 331 Ma, displaying a wide age range. The large variation of ages indicates that the zircon has inheritance or lead loss, which complicates the interpretation of the U–Pb ages. To identify inheritable zircon and grains that have undergone Pb loss, all data were processed using cumulative probability plots. On the cumulative probability plots, the U–Pb ages of the main population distributed as a nearly straight line with a positive slope. Old U–Pb outliers and young U–Pb outliners were interpreted to be inheritable and have suffered Pb loss, respectively (e.g., Harris et al., 2004; Liang et al., 2006). The U–Pb ages of the main population were obtained by removing grains from both ends until the tails have a gradient equal to or lower than the main population. Based on the method and shown in the inset figure of Fig. 4, six inheritable ages and two Pb-loss ages are omitted. A weighted average age for the remaining 24 U–Pb data is obtained as 313 ± 3 Ma, SMWD = 1.9 (Fig. 4). The U–Pb age of the main population was interpreted to be crystallization age of the intrusion.

Zircon is a resistant mineral, whereas Ti-in-zircon is a sensitive thermometer indicator for the temperature dependant incorporation of Ti^{4+} into crystallizing zircon (Watson et al., 2006). Trace ele-

Table 1
Major (wt.%) and trace element (ppm) data for the Wuling hornblende gabbro.

Sample	13WL-6 Fine-grained	13WL-7 Medium-grained	13WL-8 Medium-grained	13WL-9 Medium-grained	13WL-10 Coarse-grained	13WL-11 Coarse-grained	13WL-12 Fine-grained	13WL-13 Fine-grained
SiO_2	38.8	53.5	42.9	49.7	50.3	49.3	50.5	50.5
TiO_2	1.87	0.31	1.50	0.47	0.69	0.66	0.99	0.75
Al_2O_3	13.4	17.3	16.7	22.7	17.4	16.5	18.3	15.6
$Fe_2O_3^T$	21.8	6.30	16.0	6.57	8.58	9.58	9.41	10.1
MnO	0.20	0.13	0.17	0.10	0.14	0.15	0.17	0.19
MgO	7.23	6.38	6.51	4.38	6.20	7.81	4.34	6.46
CaO	12.7	9.97	12.7	11.8	11.9	12.2	10.2	10.1
Na_2O	1.13	3.61	1.62	2.83	2.92	2.18	3.47	2.61
K_2O	0.11	0.20	0.22	0.24	0.31	0.26	0.31	0.39
P_2O_5	0.05	0.17	0.08	0.06	0.09	0.08	0.24	0.07
LOI	2.38	1.16	1.42	1.13	1.22	1.09	1.36	2.10
Total	99.6	99.0	99.9	99.9	99.7	99.8	99.2	99.0
A/CNK	0.54	0.71	0.64	0.86	0.65	0.63	0.74	0.68
Mg#	43.6	70.2	48.7	60.8	62.7	65.5	51.8	59.8
Sc	90.5	44.2	70.8	24.5	30.2	67.8	52.9	65.8
V	1130.7	112.4	648.6	169.0	255.9	223.3	245	273.6
Cr	14.2	32.4	25.2	20.6	98.3	33.4	29.2	33.6
Co	77.4	16.0	41.3	18.6	28.2	33.8	35.0	32.0
Ni	18.5	12.1	25.4	22.4	34.6	46.0	12.2	25.1
Mn	1495.8	938.7	1268.1	666.2	1026.5	1107.6	1292.9	1458.7
Cu	211.9	10.5	227.4	31.3	123.8	178.7	292.4	113.1
Zn	96.9	36.5	59.1	27.6	44.7	50.9	67.8	71.3
Ga	17.8	12.0	18.1	17.6	15.4	14.5	19.5	16.5
Ge	3.98	1.65	3.17	1.62	2.08	1.90	2.32	2.56
Cs	0.49	0.24	0.50	0.51	0.27	1.42	0.29	0.42
Rb	2.43	2.46	4.21	5.57	0.82	4.97	5.53	11.1
Ba	23.57	59.05	37.45	57.34	63.30	60.82	90.35	76.92
Th	0.29	0.80	0.37	1.00	0.40	0.74	0.66	1.03
U	0.09	0.23	0.15	0.26	0.30	0.24	0.19	0.27
Nb	0.53	0.83	0.95	1.02	1.15	1.11	2.00	1.95
Ta	0.05	0.07	0.08	0.09	0.10	0.09	0.14	0.14
La	1.54	3.52	2.64	3.34	2.87	3.28	5.73	4.64
Ce	4.18	8.69	6.54	7.58	7.33	8.48	14.1	11.7
Pb	1.68	3.48	1.66	1.65	1.93	1.54	1.89	1.98
Pr	0.66	1.25	0.94	1.00	1.11	1.28	2.02	1.67
Sr	218.2	353.0	325.7	420.2	298	282.6	395	264.9
Nd	3.56	6.07	4.54	4.37	5.38	6.37	10.0	8.19
Zr	14.1	31.3	21.2	27.5	52.2	28.6	24.6	37.2
Hf	0.54	0.92	0.73	0.86	1.38	1.03	0.85	1.21
Sm	1.21	1.72	1.30	1.09	1.57	1.89	2.85	2.44
Eu	0.46	0.80	0.52	0.54	0.63	0.70	1.25	0.96
Ti	10,597	1723	8621	2670	3878	3914	5877	4511
Gd	1.53	2.05	1.58	1.22	1.84	2.27	3.30	2.90
Tb	0.28	0.37	0.28	0.21	0.35	0.42	0.58	0.54
Dy	1.78	2.34	1.80	1.32	2.29	2.74	3.62	3.51
Y	8.48	11.9	9.00	6.88	8.94	13.9	17.6	17.8
Ho	0.39	0.51	0.39	0.29	0.51	0.61	0.77	0.78
Er	1.02	1.41	1.07	0.80	1.40	1.65	2.05	2.16
Tm	0.14	0.20	0.15	0.12	0.20	0.24	0.29	0.32
Yb	0.90	1.31	0.97	0.78	1.33	1.56	1.80	2.08
Lu	0.14	0.21	0.15	0.12	0.20	0.24	0.27	0.33
ΣREE	17.8	30.4	22.9	22.8	27.0	31.7	48.6	42.3
$(La/Yb)_N$	214	251	306	525	213	171	193	122.92
$(La/Sm)_N$	181	205	250	387	190	150	139	108.48
$(Gd/Yb)_N$	10369	1226	8094	3337	2768	2372	2868	2093
δEu	4.55	5.60	4.43	4.04	4.81	5.78	3.30	4.66

ment data of the zircon that were analyzed for U–Pb isotopes are listed in Table 2. Ti contents of studied zircon grains are low (5.3–11.8 ppm), with an average of 8.7 ppm. Based on the Ti-in-zircon thermometer which is suitable for rocks without rutile and/or quartz (Ferry and Watson, 2007), apparent temperatures are 751–833 °C, with an average value of 799 °C, assuming a_{SiO2} and a_{TiO2} are 1 and 0.5, respectively. Taking the uncertainties of the formula into account, the maximum apparent temperatures are 786–872 °C, with an average value of 837 °C.

The analytical results of Lu–Hf isotopic compositions are listed in Table 3. Thirty-two analyses of magmatic zircon from sample 13WL yield $^{176}Lu/^{177}Hf$ ratios varying from 0.000809 to 0.003563, $^{176}Hf/^{177}Hf$ ratios from 0.282688 to 0.282893. When calculated by the crystallization age (313 Ma) of the pluton, the $\varepsilon_{Hf}(t)$ values of zircon vary from 3.5 to 10.8, and the depleted mantle Hf model ages ($T_{DM}1$) from 524 to 821 Ma, average 658 Ma, the two-stage Hf model ages ($T_{DM}2$) from 640 to 1101 Ma, average 852 Ma.

4.3. Geochemistry of the Wuling hornblende gabbro

4.3.1. Major and trace element characteristics

The major and trace elemental compositions of eight hornblende gabbro samples from Wuling are listed in Table 1. The contents of SiO_2 and $Na_2O + K_2O$ vary from 38.8 wt.% to 53.5 wt.% and 1.24 wt.% to 3.81 wt.%, respectively. On a total alkalis versus silica (TAS) diagram (Fig. 5a), these samples mainly plot in the gabbro

Table 2
Laser ablation ICP-MS zircons U–Pb data and Ti-in-zircon temperature from the Wuling hornblende gabbro.

Sample spot	Concentration and ratio				Isotope ratios						Apparent ages (Ma)						Ti (ppm)	T (°C)
	Pb	Th	U	Th/U	$^{207}Pb/^{206}Pb$	±σ	$^{207}Pb/^{235}U$	±σ	$^{206}Pb/^{238}U$	±σ	$^{207}Pb/^{206}Pb$	±σ	$^{207}Pb/^{235}U$	±σ	$^{206}Pb/^{238}U$	±σ		
13WL@1	9.1	96	133	0.73	0.0473	0.0027	0.3330	0.0190	0.0513	0.0008	61.2	129.6	291.9	14.5	322.4	5.0	7.6	787
13WL@2	11.8	124	180	0.69	0.0466	0.0026	0.3152	0.0173	0.0490	0.0006	27.9	138.9	278.2	13.4	308.5	3.9	11.3	758
13WL@3	10.4	96	155	0.62	0.0508	0.0024	0.3523	0.0162	0.0503	0.0007	235.3	109.2	306.5	12.2	316.4	4.2	8.8	734
13WL@4	14.9	157	202	0.78	0.0519	0.0023	0.3831	0.0165	0.0533	0.0006	283.4	106.5	329.3	12.1	334.7	4.0	9.5	741
13WL@5	14.2	121	211	0.57	0.0492	0.0022	0.3492	0.0151	0.0513	0.0008	166.8	101.8	304.1	11.4	322.6	4.6	10.9	755
13WL@6	12.9	145	181	0.80	0.0481	0.0024	0.3367	0.0163	0.0508	0.0007	105.6	111.1	294.7	12.4	319.4	4.3	8.2	728
13WL@7	8.9	77	140	0.55	0.0507	0.0029	0.3360	0.0190	0.0481	0.0008	227.8	126.8	294.1	14.4	302.8	4.8	9.6	742
13WL@8	11.4	88	173	0.51	0.0539	0.0027	0.3717	0.0179	0.0502	0.0008	364.9	113.0	320.9	13.2	315.9	4.8	8.6	732
13WL@9	7.4	82	110	0.74	0.0544	0.0032	0.3714	0.0217	0.0493	0.0008	387.1	136.1	320.7	16.0	310.3	5.1	8.7	733
13WL@10	11.9	111	176	0.63	0.0555	0.0025	0.3875	0.0175	0.0501	0.0007	431.5	101.8	332.5	12.8	315.4	4.1	8.4	730
13WL@11	17.5	129	270	0.48	0.0551	0.0022	0.4007	0.0158	0.0522	0.0008	416.7	88.9	342.1	11.5	328.2	4.6	11.6	760
13WL@12	12.5	159	172	0.93	0.0539	0.0026	0.3815	0.0186	0.0509	0.0008	368.6	109.2	328.2	13.7	320.3	5.0	8.6	732
13WL@13	10.1	90	156	0.58	0.0560	0.0027	0.3786	0.0178	0.0485	0.0007	453.8	105.5	326.0	13.1	305.2	4.2	9.7	743
13WL@14	12.8	146	181	0.81	0.0551	0.0025	0.3786	0.0164	0.0495	0.0007	416.7	100.0	326.0	12.1	311.7	4.2	7.9	724
13WL@15	16.9	202	240	0.84	0.0530	0.0022	0.3580	0.0143	0.0487	0.0005	331.5	94.4	310.7	10.7	306.3	3.4	10.5	751
13WL@16	18.1	212	249	0.85	0.0523	0.0023	0.3734	0.0163	0.0513	0.0006	298.2	100.0	322.2	12.0	322.4	3.7	10.1	747
13WL@17	6.2	58	91	0.65	0.0560	0.0037	0.3762	0.0234	0.0497	0.0008	450.0	146.3	324.2	17.3	312.4	5.1	6.4	706
13WL@18	10.3	102	141	0.73	0.0539	0.0027	0.3851	0.0192	0.0519	0.0008	368.6	110.2	330.8	14.1	326.0	5.1	7.5	720
13WL@19	17.3	206	239	0.86	0.0542	0.0026	0.3649	0.0164	0.0488	0.0006	376.0	73.1	315.9	12.2	307.4	3.9	10.8	754
13WL@20	7.9	75	107	0.70	0.0573	0.0033	0.4070	0.0227	0.0522	0.0010	501.9	132.4	346.7	16.4	328.1	6.0	5.3	690
13WL@21	6.0	45	91	0.49	0.0547	0.0034	0.3832	0.0240	0.0508	0.0010	466.7	173.1	329.4	17.6	319.4	6.1	5.8	697
13WL@22	9.3	115	137	0.84	0.0612	0.0032	0.3893	0.0193	0.0467	0.0008	655.6	113.7	333.9	14.1	294.0	5.0	9.3	739
13WL@23	9.0	85	140	0.61	0.0522	0.0031	0.3448	0.0198	0.0478	0.0007	300.1	133.3	300.8	15.0	301.1	4.5	8.7	733
13WL@24	3.9	40	58	0.69	0.0543	0.0037	0.3811	0.0273	0.0492	0.0009	388.9	147.2	327.8	20.1	309.6	5.8	7.2	716
13WL@25	10.3	112	154	0.73	0.0534	0.0029	0.3631	0.0196	0.0492	0.0008	346.4	130.5	314.6	14.6	309.3	4.8	8.9	736
13WL@26	9.1	110	132	0.84	0.0542	0.0029	0.3632	0.0193	0.0483	0.0007	388.9	120.4	314.6	14.4	304.3	4.6	7.4	719
13WL@27	9.6	96	137	0.70	0.0536	0.0026	0.3766	0.0181	0.0509	0.0008	353.8	109.2	324.6	13.3	320.3	4.9	6.9	712
13WL@28	12.5	137	167	0.82	0.0516	0.0024	0.3751	0.0174	0.0525	0.0008	333.4	100.9	323.4	12.8	330.1	4.8	8.3	729
13WL@29	22.7	320	310	1.03	0.0508	0.0019	0.3505	0.0137	0.0495	0.0007	231.6	87.0	305.1	10.3	311.6	4.1	11.8	762
13WL@30	15.1	144	227	0.64	0.0531	0.0023	0.3606	0.0150	0.0492	0.0006	344.5	96.3	312.7	11.2	309.9	3.6	10.7	753
13WL@31	10.8	76	162	0.47	0.0533	0.0026	0.3867	0.0196	0.0524	0.0009	342.7	113.9	332.0	14.3	329.0	5.7	6.7	710
13WL@32	6.7	56	105	0.53	0.0495	0.0030	0.3360	0.0203	0.0498	0.0009	172.3	137.9	294.1	15.4	313.2	5.5	7.6	721

Table 3
Zircon Hf isotope data for the Wuling hornblende gabbro.

Sample	$^{176}Lu/^{177}Hf$	$^{176}Hf/^{177}Hf$	2σ	$(^{176}Hf/^{177}Hf)_i$	$(^{176}Hf/^{177}Hf)_{CHUR}$	$\varepsilon_{Hf}(0)$	$\varepsilon_{Hf}(t)$	$f_{(Lu/Hf)}$	$T_{DM}1$ (Ma)	$T_{DM}2$ (Ma)
13WL@1	0.001112	0.282807	0.000013	0.282801	0.282577	1.25	7.91	−1.0	633	820
13WL@2	0.002055	0.282893	0.000014	0.282881	0.282577	4.28	10.7	−0.9	524	640
13WL@3	0.001184	0.282764	0.000014	0.282757	0.282577	−0.27	6.37	−1.0	695	918
13WL@4	0.001411	0.282811	0.000012	0.282802	0.282577	1.37	7.96	−1.0	633	817
13WL@5	0.001497	0.282780	0.000014	0.282772	0.282577	0.30	6.87	−1.0	678	886
13WL@6	0.001363	0.282851	0.000014	0.282843	0.282577	2.80	9.41	−1.0	574	725
13WL@7	0.000972	0.282835	0.000011	0.282829	0.282577	2.21	8.90	−1.0	592	757
13WL@8	0.002629	0.282737	0.000012	0.282721	0.282577	−1.25	5.09	−0.9	764	1000
13WL@9	0.001530	0.282817	0.000011	0.282808	0.282577	1.59	8.16	−1.0	626	804
13WL@10	0.001429	0.282840	0.000013	0.282832	0.282577	2.42	9.01	−1.0	591	750
13WL@11	0.002010	0.282843	0.000011	0.282831	0.282577	2.51	8.98	−0.9	597	752
13WL@12	0.003199	0.282771	0.000014	0.282752	0.282577	−0.03	6.19	−0.9	725	930
13WL@13	0.001298	0.282834	0.000011	0.282826	0.282577	2.18	8.80	−1.0	598	764
13WL@14	0.003563	0.282757	0.000016	0.282736	0.282577	−0.54	5.60	−0.9	754	967
13WL@15	0.001421	0.282810	0.000010	0.282801	0.282577	1.33	7.92	−1.0	635	819
13WL@16	0.001575	0.282757	0.000012	0.282748	0.282577	−0.53	6.03	−1.0	713	940
13WL@17	0.001679	0.282732	0.000014	0.282722	0.282577	−1.43	5.11	−0.9	752	998
13WL@18	0.001183	0.282752	0.000013	0.282745	0.282577	−0.72	5.92	−1.0	713	947
13WL@19	0.001925	0.282754	0.000014	0.282743	0.282577	−0.62	5.86	−0.9	724	951
13WL@20	0.001801	0.282777	0.000012	0.282767	0.282577	0.18	6.70	−0.9	688	897
13WL@21	0.001102	0.282818	0.000011	0.282811	0.282577	1.62	8.28	−1.0	618	797
13WL@22	0.001107	0.282797	0.000011	0.282790	0.282577	0.88	7.53	−1.0	648	844
13WL@23	0.001221	0.282800	0.000012	0.282793	0.282577	1.00	7.63	−1.0	645	838
13WL@24	0.001494	0.282853	0.000011	0.282844	0.282577	2.86	9.44	−1.0	574	723
13WL@25	0.001173	0.282774	0.000012	0.282767	0.282577	0.07	6.71	−1.0	681	896
13WL@26	0.001955	0.282688	0.000018	0.282676	0.282577	−2.99	3.49	−0.9	821	1101
13WL@27	0.001361	0.282846	0.000010	0.282838	0.282577	2.63	9.24	−1.0	581	736
13WL@28	0.001462	0.282750	0.000013	0.282741	0.282577	−0.78	5.80	−1.0	721	954
13WL@29	0.003399	0.282828	0.000016	0.282808	0.282577	1.99	8.17	−0.9	642	804
13WL@30	0.001654	0.282785	0.000011	0.282775	0.282577	0.44	6.99	−1.0	675	879
13WL@31	0.001507	0.282770	0.000015	0.282761	0.282577	−0.07	6.50	−1.0	693	910
13WL@32	0.000809	0.282861	0.000017	0.282856	0.282577	3.15	9.87	−1.0	552	695

Note: [$(^{176}Lu/^{177}Hf)_{CHUR}$ = 0.0332 ± 2, $(^{176}Hf/^{177}Hf)_{CHUR(0)}$ = 0.282772 ± 29 (Blichert-Toft and Albarede, 1997); $(^{176}Lu/^{177}Hf)_{DM}$ = 0.0384, $(^{176}Hf/^{177}Hf)_{DM}$ = 0.28325 (Griffin et al., 2000)] was used for the calculations. $\lambda_{Lu\text{-}Hf} = 1.867 \times 10^{-11}$ year^{-1} $\varepsilon_{Hf}(t)$, $T_{DM}1$ and $T_{DM}2$ of samples 13WL were calculated using the age of 313 Ma.

Table 4
Whole rock Sr–Nd isotopic data of the Wuling hornblende gabbro.

Sample	Rb (ppm)	Sr (ppm)	Sm (ppm)	Nd (ppm)	$^{87}Rb/^{86}Sr$	$^{87}Sr/^{86}Sr$	2σ	$(^{87}Sr/^{86}Sr)_i$	$\varepsilon_{Sr}(t)$	$^{147}Sm/^{144}Nd$	$^{143}Nd/^{144}Nd$	2σ	$(^{143}Nd/^{144}Nd)_i$	$\varepsilon_{Nd}(t)$	$T_{DM}2$ (Ma)
13WL-6	2.4	218	1.2	3.6	0.032	0.704641	0.000007	0.704497	5.1	0.205	0.512845	0.000006	0.512423	3.7	772
13WL-7	2.5	353	1.7	6.1	0.020	0.704641	0.000007	0.704551	5.9	0.171	0.512758	0.000004	0.512406	3.4	800
13WL-8	4.2	326	1.3	4.5	0.037	0.704641	0.000007	0.704474	4.8	0.173	0.512749	0.000005	0.512393	3.1	820
13WL-9	5.6	420	1.1	4.4	0.038	0.704641	0.000007	0.704470	4.7	0.150	0.512688	0.000005	0.512379	2.8	841
13WL-10	0.8	298	1.6	5.4	0.008	0.704641	0.000007	0.704606	6.7	0.176	0.512778	0.000004	0.512416	3.6	783
13WL-11	5.0	283	1.9	6.4	0.051	0.704641	0.000007	0.704414	4.0	0.179	0.512800	0.000005	0.512431	3.9	759
13WL-12	5.5	395	2.9	10.0	0.041	0.704641	0.000007	0.704460	4.6	0.172	0.512761	0.000004	0.512408	3.4	796
13WL-13	11.1	265	2.4	8.2	0.121	0.704641	0.000007	0.704098	−0.5	0.180	0.512776	0.000004	0.512406	3.4	800

Note: [$(^{87}Rb/^{86}Sr)_{CHUR}$ = 0.0847 (Mcculloch and Black, 1984); $(^{87}Sr/^{86}Sr)_{CHUR}$ = 0.7045 (DePaolo, 1988); $(^{147}Sm/^{144}Nd)_{CHUR}$ = 0.1967 (Jacobsen and Wasserburg, 1980); $(^{143}Nd/^{144}Nd)_{CHUR}$ = 0.512638 (Goldstein et al., 1984)] was used for the calculations. $\lambda_{Rb} = 1.42 \times 10^{-11}$ year^{-1}; $\lambda_{Sm} = 6.54 \times 10^{-12}$ year^{-1}. Both $\varepsilon_{Nd}(t)$ and $\varepsilon_{Sr}(t)$ were calculated using the age of 313 Ma.

field, except for 13WL-6 and 13WL-8. Among them, sample 13WL-6 and 13WL-8 have particularly low SiO_2 content (38.8 wt.% and 42.9 wt.%), high Fe_2O_3T content (21.8 wt.% and 16.0 wt.%) and high TiO_2 content (1.87 wt.% and 1.50 wt.%), which is consistent with the high content of Fe-oxide in the two samples. Considering SiO_2 and Fe_2O_3T as a whole, all the analyzed samples have almost the same content, narrowly ranging from 56.2 wt.% to 60.7 wt.%. Meanwhile, they show highly consistent trace element normalized pattern which we will discuss it in a later section, indicating the same magma source. Aluminum saturation index (A/CNK = mol $Al_2O_3/(CaO + Na_2O + K_2O)$) ranges from 0.54 to 0.86. Mg values ($Mg^{\#}$ = mol $Mg^{2+}/(Mg^{2+} + Fe^{2+})$) vary from 44 to 70. On the AFM ($Na_2O + K_2O$–FeO_T–MgO) triangle diagram (Fig. 5b), all the points are ploted along the tholeiite magma evolution trend. In the K_2O vs. SiO_2 diagram (Fig. 5c), the samples mainly fall in the low–K region.

Total rare earth element (ΣREE) contents of the hornblende gabbro are relatively low, varying from 17.8 ppm to 48.6 ppm, with $(La/Yb)_N$ values from 1.23 to 3.08, $(La/Sm)_N$ values from 0.82 to 1.98, $(Gd/Yb)_N$ values from 1.15 to 1.41 and δEu values from 1.03 to 1.44 (Table 1). These ratios show that there is minor REE fractionation and LREEs are slightly enriched (Fig. 6a). Eu positive anomaly is consistent with the presence of plagioclase cumulate. Contents of the large ion lithophile element (LILE) vary from 1.54 ppm to 3.48 ppm for Pb and 218 ppm to 420 ppm for Sr (Table 1). These LILE are highly enriched as is shown in trace element spider diagram (Fig. 6c). Contents of the high field strength elements (HFSE) vary from 0.53 ppm to 2.00 ppm for Nb, 0.05 ppm to 0.14 ppm for Ta, 14.1 ppm to 52.2 ppm for Zr, 0.54 ppm to 1.38 ppm for Hf, 1723 ppm to 10,597 ppm for Ti (Table 1). Among these HFSE, Nb and Ta are strongly depleted and Zr, Hf and Ti are slightly depleted (Fig. 6c). For sample

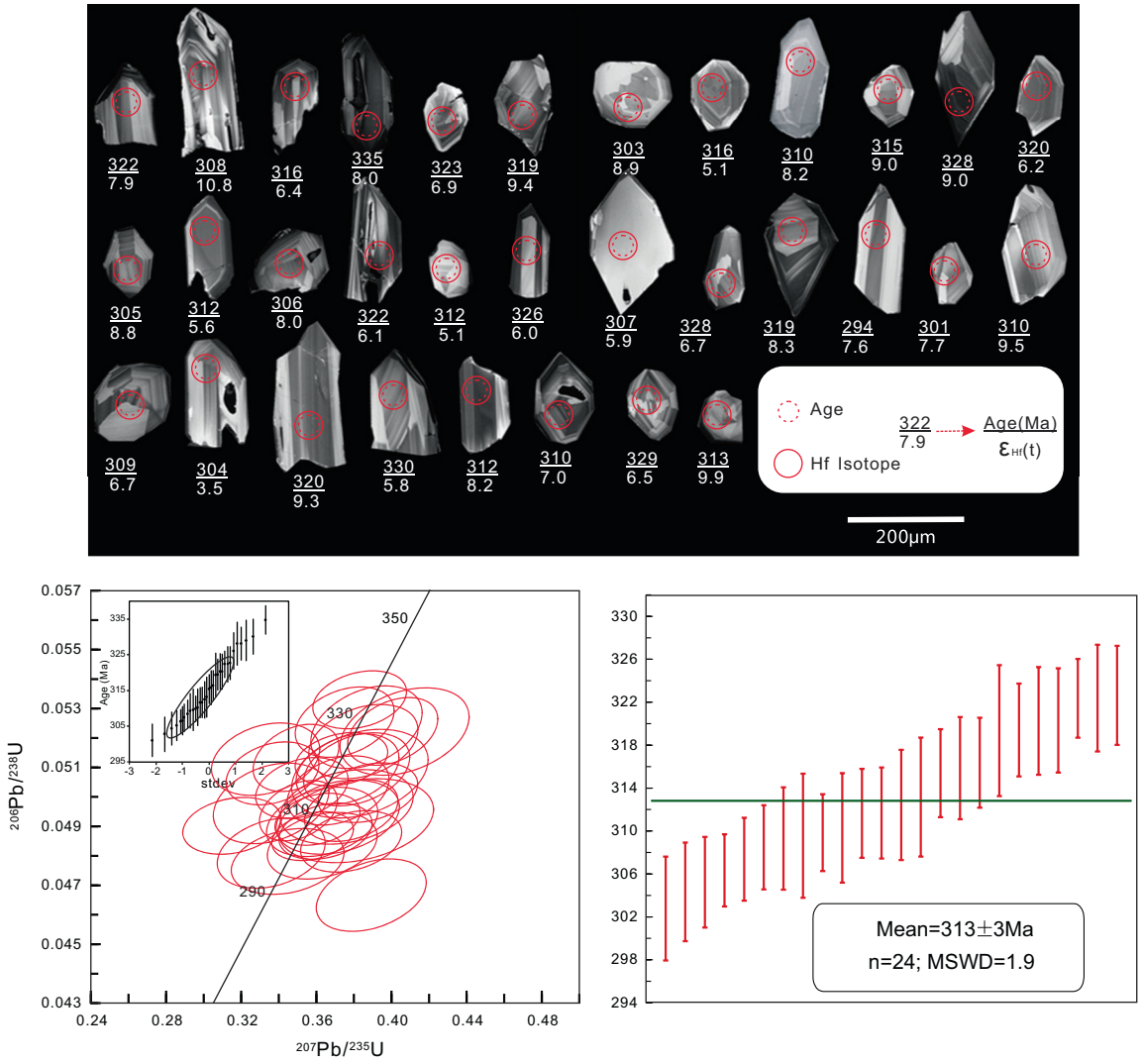

Fig. 4. CL images and concordia diagrams for analyzed zircon grains from the Wuling hornblende gabbro. Circles indicate the locations of analyzed sites. The inset is cumulative probability plot to rule out zircon grains have inheritance and lead loss.

13WL-6 and 13WL-8, their slight Ti enrichment is consistent with high content of Fe–Ti oxides in these two samples.

4.3.2. Sr–Nd isotope characteristics

Whole rock Sr–Nd isotope compositions of the eight Wuling gabbro samples are listed in Table 4 and ploted in Fig. 10a. The studied rock has a small range of initial Sr isotope ratios (0.7043–0.7049) and positive $\varepsilon_{Nd}(t)$ values (at 313 Ma) (2.8–3.9), showing Sr–Nd isotopic values characteristic of lithospheric mantle melting.

5. Discussion

5.1. Effect of alteration and crust contamination

Based on petrographic observation and variable LOIs (loss on ignitions) (1.09–2.38) listed in Table 1, the secondary minerals in the Wuling hornblende gabbro are predominantly chlorite and a small amount of sericite, implying that the Wuling hornblende gabbro may have undergone low-grade metamorphism or variable degrees of alteration after emplacement. Thus, the potential effects of these processes are assessed prior to further petrogenetic analysis. Generally, the major elements Al, Ti, Fe, P, the HFSEs, REEs (except Ce and Eu) and transition metals are least sensitive to mobility whereas the major elements Na, K, Ca, and the LILEs may be mobile during the post-magmatic alteration and greenschist to amphibolite facies metamorphism (Winchester and Floyd, 1977; Rollinson, 1993; Hawkesworth et al., 1997; Polat et al., 2002; Polat and Hofmann, 2003). LREEs are more sensitive to secondary processes in comparison with MREEs and HREEs, however, the mobility of REE only occurs at high water/rock ratio or during carbonatization (Humphris, 1984), which is not observed in our case.

Chemical effects of alteration are primarily reflected in an unsystematic variation of whole-rock K_2O/Na_2O ratios and the decoupling of LILE, as indicated by the relative depletion of Rb in comparison with Ba (Altherr et al., 2008). As for the Wuling hornblende gabbro, the K_2O/Na_2O ratio range (0.06–0.15) is relatively narrow, and both Rb and Ba are positively correlated with K_2O (Fig. 7), implying the limited effect of the late alteration on K, Na and LILEs of the whole rock. The altered basalts tend to have high Ba abundance and abnormally high Ba/Rb and Ba/Nb (Price et al., 1991; Zhang and O'Reilly, 1997), though not showing Rb and K depletions (Zhang and O'Reilly, 1997). Conversely, the unaltered basalts do not simultaneously possess high Ba/Nb and high Ba/

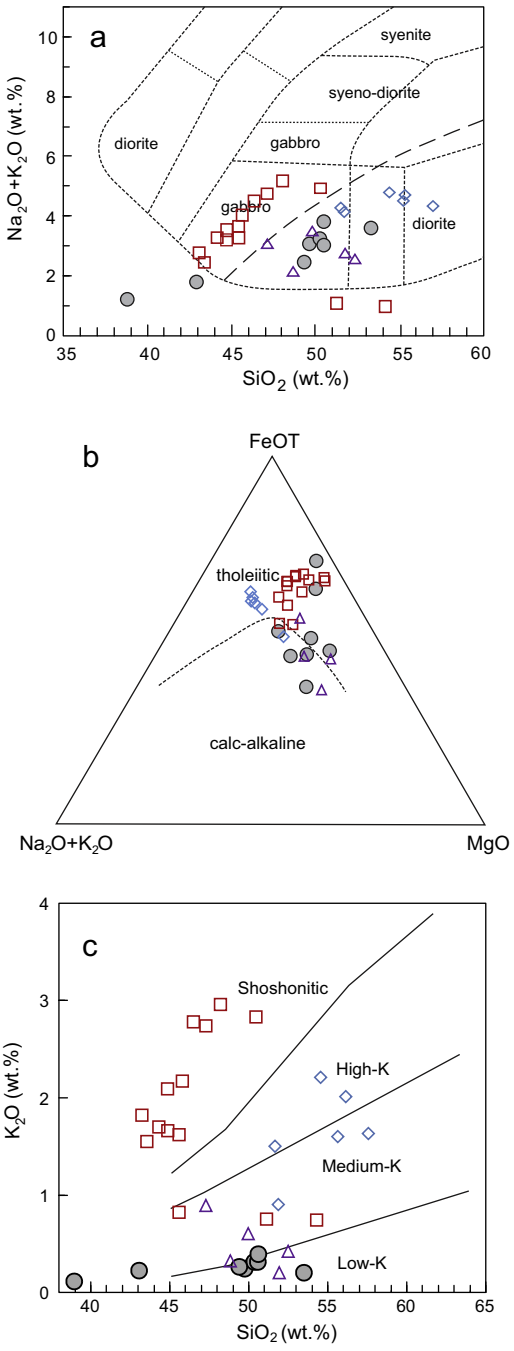

Fig. 5. Rock classification diagrams: (a) Total alkalis versus silica (TAS) diagram (after Maitre et al., 1989), (b) MgO–FeOt–$Na_2O + K_2O$ diagram (after Irvine and Baragar, 1971), (c) K_2O vs. SiO_2 diagram (after Peccerillo and Taylor, 1976). The Wuling gabbro: gray solid circle; the Chagangnuoer Fe-rich basalt: red hollow square; the Zhongyangchang mafic dike: the blue hollow diamond; the Muhan-basitao gabbro: the purple hollow triangle. The compared data are from Li et al. (2015b), Liu et al. (2012) and Tang et al. (2014). (For interpretation of the references to color in this figure legend, the reader is referred to the web version of this article.)

Rb. The Wuling hornblende gabbro has a narrow range of low Ba/Rb (6.91–24.0, except for sample 13WL-10) despite their variable but high Ba/Nb (39.4–70.9). Therefore, the Ba, Nb and Rb distributions observed from the Wuling hornblende gabbro reflect geochemical or mineralogical signatures of the mantle source rather than post-magmatic alteration.

Crustal contamination is almost inevitable when mantle-derived magmas ascend through continental crust or evolve within a crustal magma chamber (Watson, 1982; Castillo et al., 1999). Given that crustal components generally are characterized by high $^{87}Sr/^{86}Sr$ and Rb/Sr ratios and SiO_2 contents, and distinctly low $\varepsilon_{Nd}(t)$ and MgO, Nb–Ta contents (Rudnick and Fountain, 1995), any crustal contamination during magma ascent would have caused an increase in $(^{87}Sr/^{86}Sr)_i$ and a decrease in $\varepsilon_{Nd}(t)$ in the magma suites (Rogers et al., 2000). As is shown in Fig. 8a, the Rb/Sr ratio of the Wuling hornblende gabbro has a relatively large range from 0.003 to 0.042 while the $(^{87}Sr/^{86}Sr)_i$ values are nearly constant (0.7043–0.7049). With the increasing of the Rb/Sr ratio, $(^{87}Sr/^{86}Sr)_i$ ratio does not increase obviously, suggesting that the effect of the crustal contamination is insignificant and the variation of Rb/Sr and $(^{87}Sr/^{86}Sr)_i$ may be attributed to the fractional crystallization process (Altunkaynak and Genc, 2008). Considering high $\varepsilon_{Nd}(t)$ (+2.8 to +3.9) and zircon $\varepsilon_{Hf}(t)$ (+3.5 to +10.8), the effect of the crustal contamination on the upwelling magma is limited. However, previous experiments have shown that the isotopic equilibrium advances faster than the elemental equilibrium (Pin and Duthou, 1990; Scherer et al., 2000; Griffin et al., 2002), and therefore whether elemental compositions were significantly affected by crustal contamination requires further analyses. The content of SiO_2, K_2O, Zr, Hf and LILEs of the basic magma increase when contaminated by the crustal materials, resulting in the increase of La/Nb ratio and the decrease of Ce/Pb (Sun et al., 2008). The La/Nb ratio of the Wuling hornblende gabbro does not increase with the increase of SiO_2 content (Fig. 8b), and meanwhile, the Ce/Pb ratio does not decrease with the increase of SiO_2 content (Fig. 8c), indicating that no obvious crustal contamination during the magma ascent. Thus, a combination of the isotopic and elemental geochemistry prompts us to infer that the crustal contamination did not play a significant role in their formation.

5.2. Fractional crystallization and crystallization process of the Wuling hornblende gabbro

The $Mg^{\#}$ values of the Wuling hornblende gabbro range from 44 to 70 (Table 1), indicating that our samples chemically represent evolved magma rather than primitive magma. The variable major and trace element compositions of the Wuling hornblende gabbro suggest that their parent magma may have undergone varying degree of fractional crystallization and crystal accumulation. The positive correlations between Cr and Ni and MgO (Fig. 9e and f) for the Wuling hornblende gabbro indicate the fractional crystallization of olivine or clinopyroxene. The positive correlation between Cr and Ni (Fig. 9h) and the broadly positive correlation between CaO and MgO (Fig. 9a) are also consistent with the fractional crystallization of clinopyroxene. The negative correlation between Al_2O_3 and MgO (Fig. 9b) and the positive Eu anomaly for the Wuling hornblende gabbro suggests a plagioclase-dominated accumulation. In addition, the increasing $Fe_2O_3^T$, TiO_2 and V with the decreasing MgO (Fig. 9c, d and g) is reflective of the fractional crystallization of Fe–Ti oxides.

The high Al_2O_3 (13.4–22.7 wt.%) and high CaO (9.97–12.7 wt.%) contents of the Wuling gabbro indicate that they are crystallized from high-alumina basaltic magma. Based on the petrography observation, the formation of the Wuling gabbro requires a two-stage process to explain its mineral composition. The early-stage minerals are predominately anhydrous minerals, including olivine, clinopyroxenes, plagioclase, magnetite and ilmenite. The heavy minerals like olivine, clinopyroxene and magnetite sink, whereas plagioclase crystals tend to float in the magma chamber, resulting in absence of olivine and the rare presence of clinopyroxenes but abundant plagioclase grains in the Wuling hornblende gabbro. This can also explain the high Fe-oxide content in some Fe-rich samples. During this stage, the plagioclase crystal is dominantly anorthite with high An of above 91 (Table S1). Consequently, the

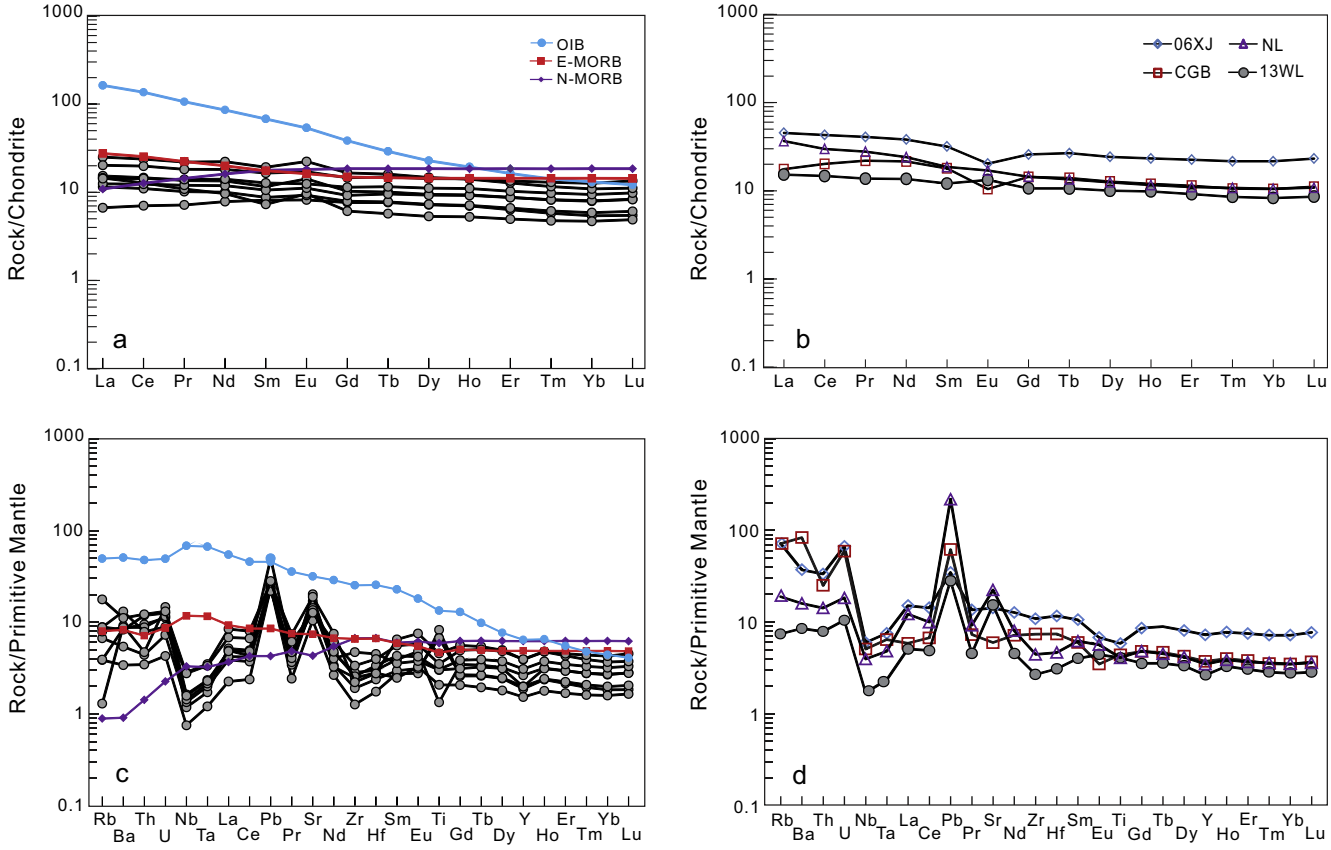

Fig. 6. (a and b) REE distribution pattern spider diagrams, (c and d) trace element distribution pattern spider diagrams. The symbols are the same to those of Fig. 5. Normalizing values, OIB, N-MORB and E-MORB data are from Sun and Mcdonough (1989).

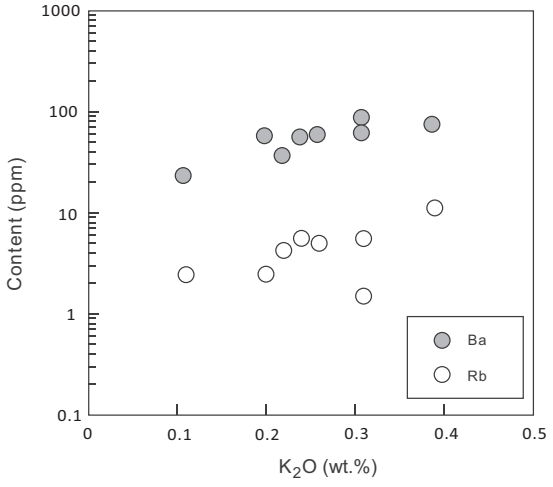

Fig. 7. Ba and Rb vs. K_2O for the Wuling hornblende gabbro.

residual melt is chemically evolved and resembles the bulk content of water-rich andesitic magma. The hydrous evolved melt reacted with the early-stage minerals and filled clearance between them. During the late stage, the crystallization of abundant hornblende favors the hydrous feature of the residual melt. Hornblende is often very large in size, occurring as enclosing grain within which small pyroxene, Fe-oxide and euhedral plagioclase grains are floating as discrete grains. This type of hornblende grain is defined as 'poikilitic hornblende' (Fig. 3d and e). At place, corrosion boundary between hornblende and plagioclase shows evident reaction relationship between the evolved melt and early-stage plagioclase (Fig. 3b). At end of this stage, the plagioclase (andesine to albite) continued to crystallize and cut the hornblende grain.

5.3. Source of the Wuling gabbro

The Wuling hornblende gabbro is subduction-related, characterized by enrichment in LILEs, LREEs and depletion in HFSEs as shown in Fig. 6a and c. The relatively positive whole rock $\varepsilon_{Nd}(t)$ values (2.8–3.9) with a Nd model ages (0.76–0.84 Ga) suggest that a depleted mantle end-member was involved in the formation of the Wuling gabbro (Fig. 10a). Meanwhile, the Wuling gabbro displays variable but positive $\varepsilon_{Hf}(t)$ values (3.5–10.8), yielding two stage Hf model ages between 0.64 Ga and 1.1 Ga (Fig. 10b), reflecting a somewhat heterogeneous mantle source. These geochemical characteristics of the Wuling gabbro resemble the features of the 314 Ma Fe-rich basalts ($(^{87}Sr/^{86}Sr)_i = 0.7046–0.7058$, $\varepsilon_{Nd}(t) = 3.0–4.7$, $T_{DM}2 = 0.9–1.4$ Ga) in the Chagangnuoer area (Li et al., 2015b) and the 310 Ma mafic dike (hornblende gabbro) ($(^{87}Sr/^{86}Sr)_i = 0.7048–0.7053$, $\varepsilon_{Nd}(t) = 2.9–3.8$) in the Zhongyangchang area (Tang et al., 2014) and the 317 Ma hornblende gabbro in the Muhanbasitao area (Liu et al., 2012) (Fig. 10a), all of which have been considered to form in an active continental margin environment.

The minor REE fractionation of the Wuling gabbro with $(La/Yb)_N$ values from 1.23 to 3.08, is distinct from the garnet REE fractionation with $Kd_{Yb}^{Grt/L}/Kd_{La}^{Grt/L} \approx 7000$, however, similar to that of spinel with $Kd_{Yb}^{Sp/L}/Kd_{La}^{Sp/L} \approx 1$ (Irving and Frey, 1978), implying a shallow spinel peridotite mantle source (Xue and Zhu, 2009). The Sm/Yb ratios of igneous rocks are sensitive to basalt source mineralogy

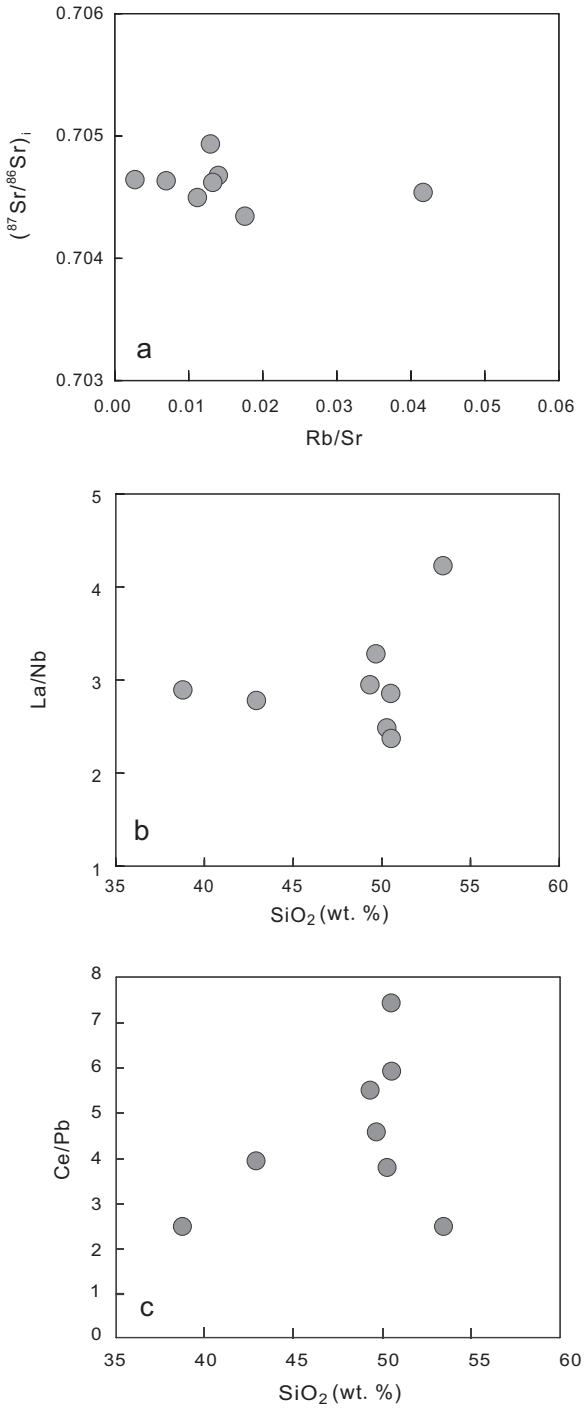

Fig. 8. (a) $(^{87}Sr/^{86}Sr)_i$ vs. Rb/Sr (after Altunkaynak and Genc, 2008), (b) La/Nb vs. SiO_2 and (c) Ce/Pb vs. SiO_2 for the Wuling hornblende gabbro.

(Keskin, 2005; Genc and Tuysuz, 2010). In the La/Sm versus Sm/Yb diagram, the spots of the Wuling gabbro are plotted between the fractional melting curve and the batch melting curve of spinel peridotite (Fig. 11a). The conclusion is further supported in the La/Yb versus Dy/Yb diagram (Fig. 11b), where the low Dy/Yb ratios along with variable La/Yb ratios of the Wuling gabbro suggest their generation at a shallow depth corresponding to the stability field of spinel peridotite (e.g., Jung et al., 2006; Manikyamba et al., 2014).

The pronounced negative Nb–Ta, Zr–Hf, Ti anomalies and high LILE/HFSE ratios of the pluton are diagnostic features of subduction-related arc magma, implying the introduction of metamorphic fluids or melts into the mantle wedge (Perfit et al., 1980; Hawkesworth et al., 1993; Pearce and Peate, 1995; Kelemen et al., 2003; Pearce, 2008). Previous investigations have shown that magmas derived from the sources modified by subducted slab-derived melts exhibit elevated Th and LREE contents relative to N-MORB as well as high Th/La (>0.2) and Th/Yb (>2) ratios (Woodhead et al., 2001; Richards and Kerrich, 2007). However, most samples of the Wuling gabbro display depletion of Th relative to Ba as well as variable Th/La (0.12–0.3, average of 0.19) and Th/Yb (0.3–1.29, 0.53 on average), indicating that the addition of subducted sediments into the magma source is insignificant. Previous studies have indicated that subducted slab-released fluids are characterized by high contents of Ba, Rb, Sr, U and Pb, leading to elevated Ba/Th, U/Th or Sr/Th ratios in the lavas (Condomines et al., 1988; Hawkesworth et al., 1997; Johnson and Plank, 2000), whereas subducted oceanic sediment-derived melts contain high concentrations of Th and LREEs with distinctly elevated Th/Ce ratios (Hawkesworth et al., 1997; Johnson and Plank, 2000; Plank, 2005). The Wuling gabbro exhibits strong enrichments of fluid-mobilized trace elements with high Sr/Th ratios (258–878) and low Th/U ratios (1.31–3.82), which is consistent with fluid-induced enrichment (Hawkesworth et al., 1997; Jiang et al., 2009). The metasomatism features of mantle source for the Wuling gabbro may be further examined through a plot of Ba/Th versus La/Sm (Labanieh et al., 2012) and Th/Yb versus Sr/Nd (Woodhead et al., 1998). As shown in Fig. 12a and b, the spots of the Wuling gabbro lie parallel to the Ba/Th axis and the Sr/Nd axis, demonstrating that the mantle source was metasomatized by aqueous fluids.

Additionally, the mineral compositions of the Wuling gabbro also imply that they are generated in water-rich environment. Hornblende and anorthitic plagioclase are common in the Wuling gabbro. The occurrence of abundant hornblende implies a 'wet' mantle source (e.g., Munteanu et al., 2010; Ma et al., 2013). Previous experiments indicate that refractory melts with high CaO/Na_2O (12–15), or melts with exceptionally high Al_2O_3 (>18 wt.%) are alternative to generate anorthite under above conditions (Panjasawatwong et al., 1995), which is inconsistent with the normal CaO/Na_2O ratios (2.8–11.2) and Al_2O_3 contents (13.4–22.3 wt.%, average 17.2 wt.%) of the Wuling gabbro. Therefore, the incorporation of fluid released from the subducted slab may lower the solidus temperature and trigger the widespread melting of refractory lithospheric mantle peridotite (Tatsumi and Eggins, 1995). Zircon is an accessory mineral coexisting with pyroxene, plagioclase and hornblende, and the crystallization temperature of it can represent the temperature at which the gabbro formed. Based on the revised Ti-in-zircon thermometers by Ferry and Watson (2007), we obtain the maximum estimated apparent temperature of the Wuling hornblende gabbro is 876 °C, which is lower than the crystallization temperature of a normal basaltic magma (>1200 °C) (Lee et al., 2009) and further supporting that the magma source of the Wuling gabbro was 'wet'.

5.4. Geodynamic implication

Generally, an intra-continent rift is developed in a post-orogenic or intra-plate extensional setting and represents the ceasing of arc magmatic activities (Zhang et al., 2007a,b; Metcalf and Shervais, 2008). The subduction-related signature of the Wuling gabbro rules out the possibility of an intra-continent rift environment in the Awulale Mountains before late Carboniferous (at least before 313 Ma). During the Late Paleozoic, Awulale Mountains could act as both a part of the southern margin and the northern margin of the YCTP and be simultaneously effected by the northward subduction of the South Tianshan Ocean and the southward subduction of the North Tianshan Ocean (Wang and Xu, 2006;

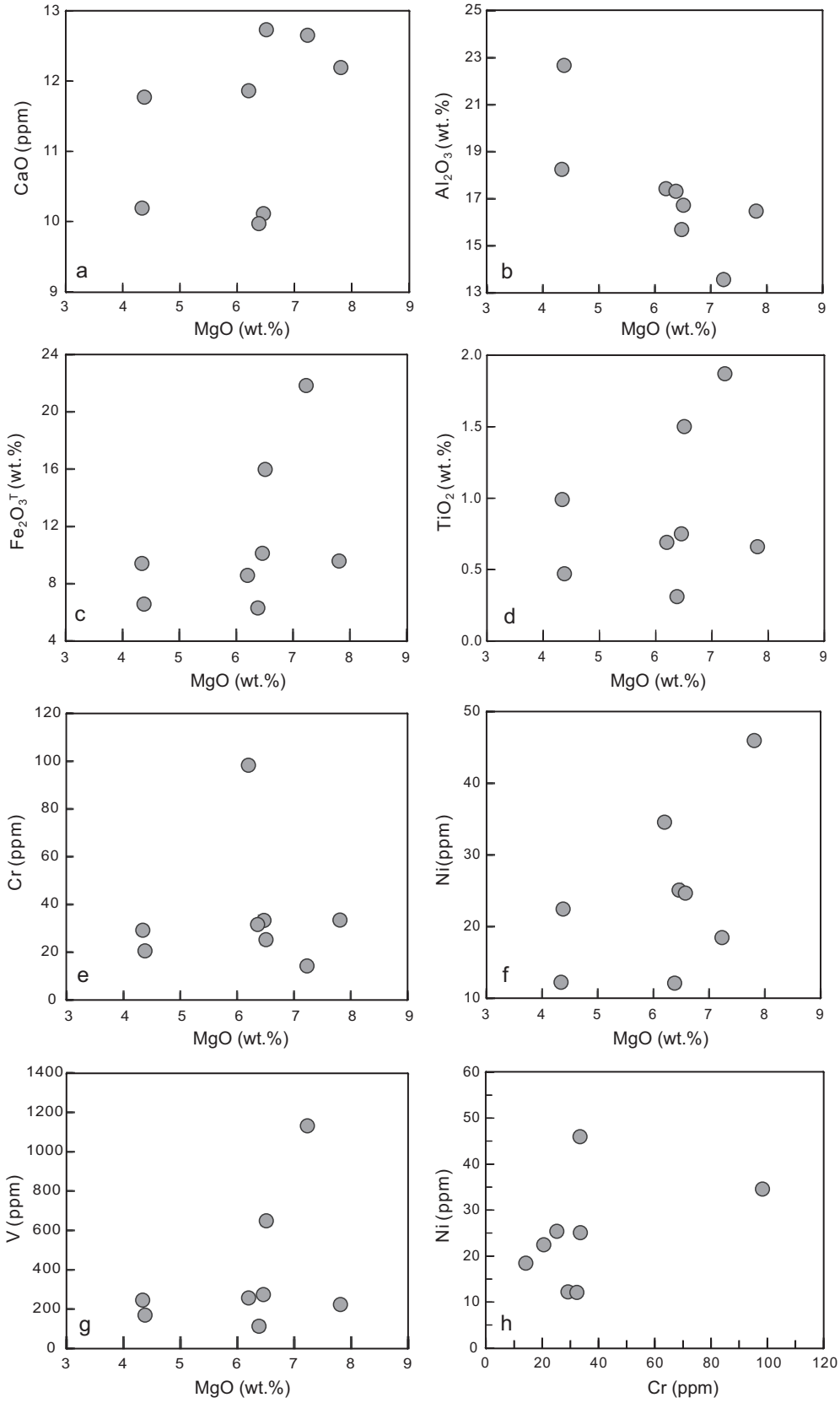

Fig. 9. Plots of representative major and trace elements of the Wuling hornblende gabbro. (a) CaO vs. MgO; (b) Al_2O_3 vs. MgO; (c) Fe_2O_3T vs. MgO; (d) TiO_2 vs. MgO; (e) Cr vs. MgO; (f) Ni vs. MgO; (g) V vs. MgO; and (h) Ni vs. Cr.

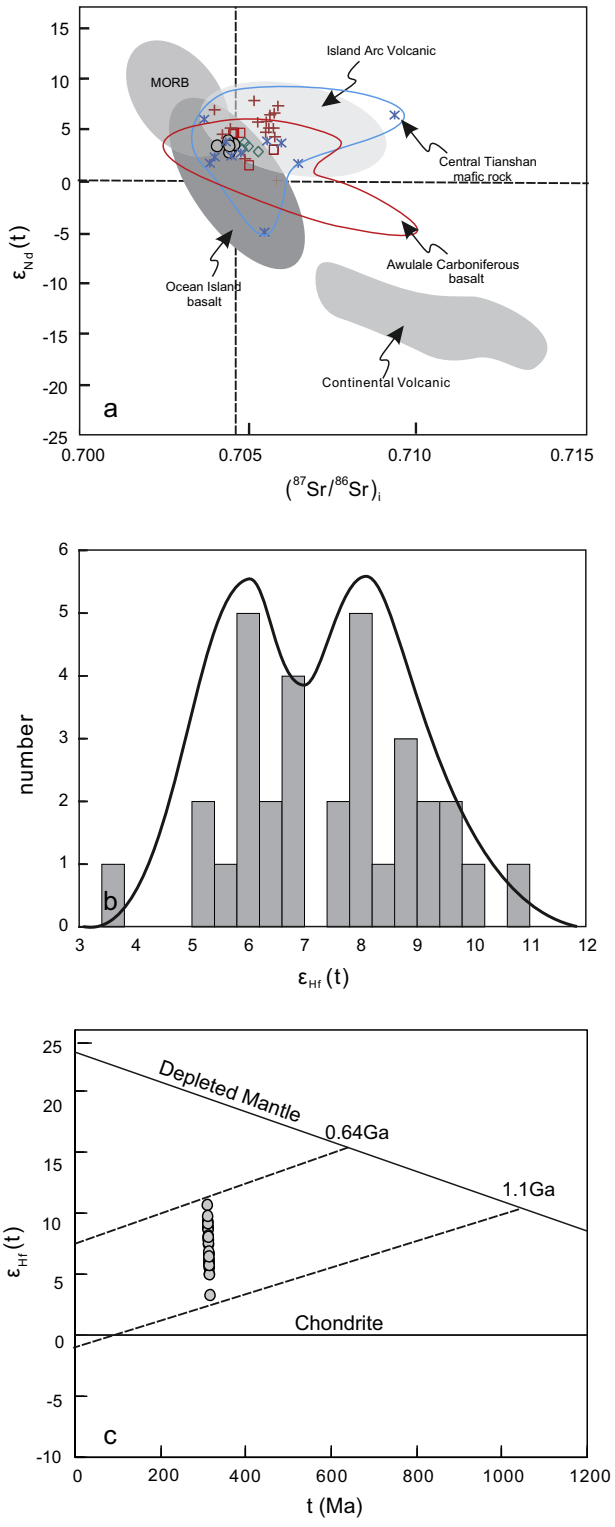

Fig. 10. (a) $\varepsilon_{Nd}(t)$ vs. $(^{87}Sr/^{86}Sr)_i$ diagram, (b) zircon Hf isotope evolution diagram for the Wuling hornblende gabbro. The symbols are the same to those of Fig. 5. Red plus sign: Luotuogou gabbro. Blue product sign: Jingbulake mafic–ultramafic rocks. Data of the central Tianshan maifc rocks are from Chen et al. (1995), Yang and Zhou (2009), Tang et al. (2012) and Yang et al. (2012). Compositions of MORB (Middle Ocean Ridge Basalt), OIB (Ocean Island Basalt), island arc volcanic and continental volcanic are form Hart et al. (1986), Zindler and Hart (1986) and Hart et al. (1992). (For interpretation of the references to colour in this figure legend, the reader is referred to the web version of this article.)

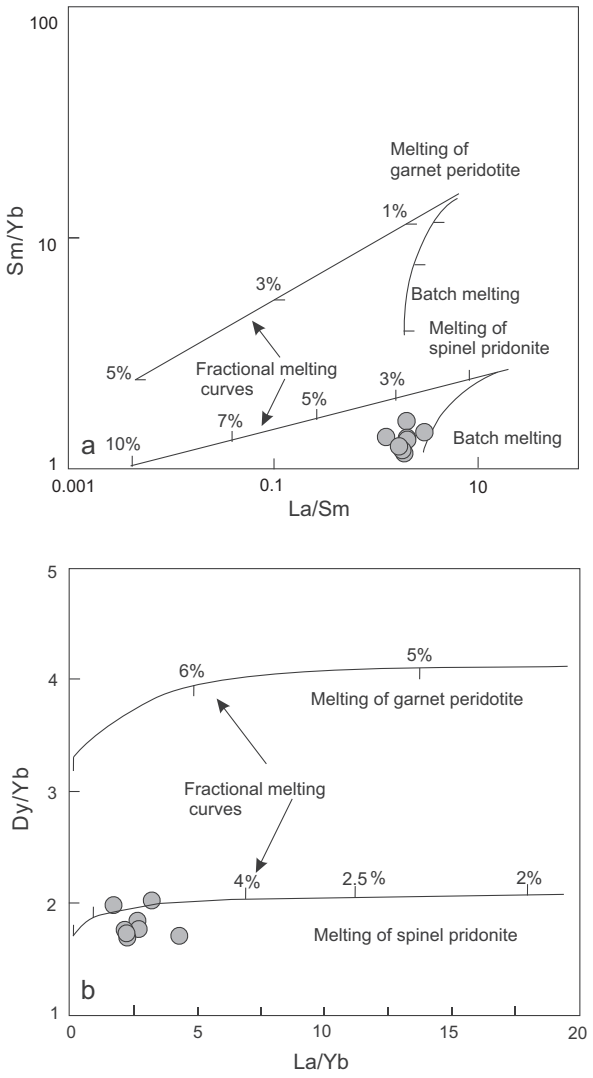

Fig. 11. (a) Sm/Yb vs. La/Sm (after Genc and Tuysuz, 2010; Keskin, 2005) and (b) Dy/Yb vs La/Yb (after Jung et al., 2006) plots for the Wuling hornblende gabbro.

Gao et al., 2009). Therefore, there is a debate on the polarity of the subduction that the Awulale orogen was mainly subjected to. Han et al. (2010) reported a SHRIMP zircon U–Pb age of 316 Ma for the Sikeshu stitching pluton which crosscuts the North Tianshan suture zone hinting that the North Tianshan Ocean had closed at the end of early Carboniferous and the collision between the Junggar Plate and the YCTP may have occurred between 325 Ma and 316 Ma. Meanwhile, a late Carboniferous collision between the Tarim Plate and the YCTB was proposed by Han et al. (2011) based on ~319 Ma high pressure peak metamorphism of subducted oceanic material from the South Tianshan Orogen and ~300 Ma stitching plutons crosscutting the suture zone. Therefore, we suggest that the formation of the Wuling gabbro was mainly controlled by northward subduction of the Southern Tianshan Ocean. The subduction-related granitoid plutons along the South Yili Block and the Central Tianshan displays a wide age range from 450 Ma to 320 Ma, indicating that the South Tianshan Ocean had been subducting northward under the YCTP during the late Silurian–early Carboniferous (Long et al., 2011). The Permian (298–251 Ma) post-subduction shoshonitic rocks (Zhao et al., 2009; Yang et al., 2012, 2014a) and the middle-late Permain underplating adakite (Xiong et al., 2001; Zhao et al., 2006, 2009) were reported in the Awulale Mountains, implying that the subduction of the South Tianshan Ocean had ceased and the Awulale Mountains had entered a post-collisional extensional environment since the Permian.

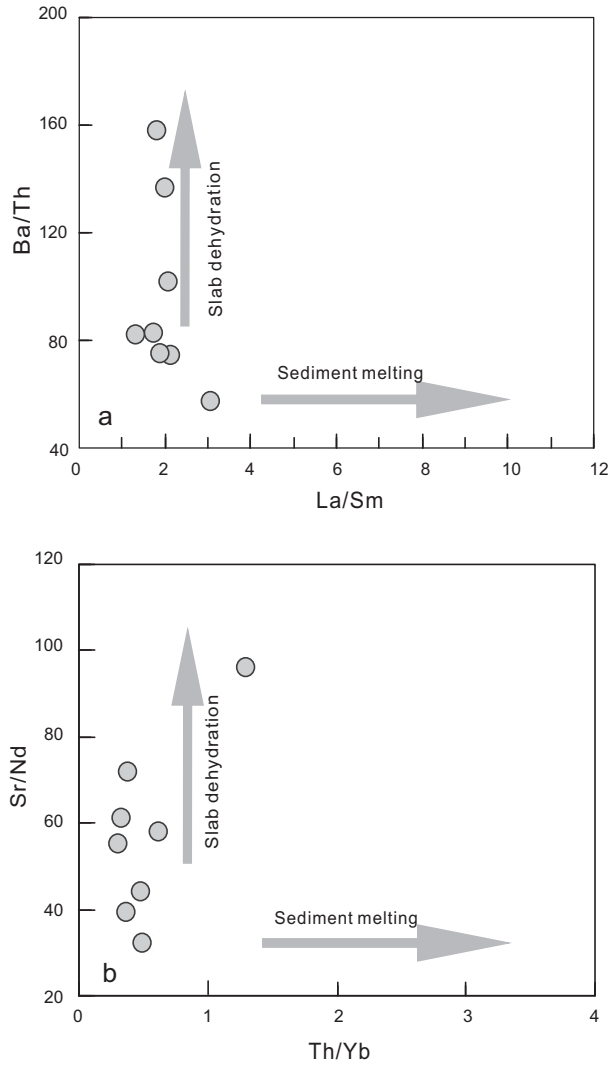

Fig. 12. (a) Ba/Th vs. La/Sm (after Labanieh et al., 2012) and (b) Th/Yb vs. Sr/Nb (after Woodhead et al., 1998) plots for the Wuling hornblende gabbro.

Magmatic rocks coeval with the Wuling gabbro are widely exposed along the Awulale orogenic belt, petrologically ranging from acidic rock series to basic rock series and including some typical rocks like I-type granite (Yan et al., 2013), trachy-andesite and basalt (Zhu et al., 2009) and rock associations like Fe-rich basalt-rhyolite associations and mafic dike-granitoid associations (Niu et al., 2011; Liu et al., 2012; Li et al., 2015b). Specially, Niu et al. (2011) and Li et al. (2015b) discovered Fe-rich basalt–rhyolite associations from the Chagangnuoer area of the eastern Awulale, suggesting a back-arc extensional setting for the generation of large-scale iron metallization along the AMB. The Fe-rich samples of the Wuling gabbro geochemically resemble the Chagangnuoer Fe-rich basalt and might also originate from a Fe-rich basaltic magma. The extensional back-arc setting provided advantageous channels for the upwelling of heavy Fe-rich basaltic magma. Additionally, mafic dike-granitoid associations are common in extensional tectonic regimes (Yang et al., 2007; Xu et al., 2008; Said and Kerrich, 2010). The late Carboniferous mafic dike-granitoid associations reported by Tang et al. (2014) and Liu et al. (2012) outcrop in the Muhanbasitao and Zhongyangchang area of the Awulale Mountains, respectively. The subduction-related signatures of these associations indicate that they are not related to a post-collisional extensional setting and a back-arc extensional setting would be a suitable environment for their emplacement.

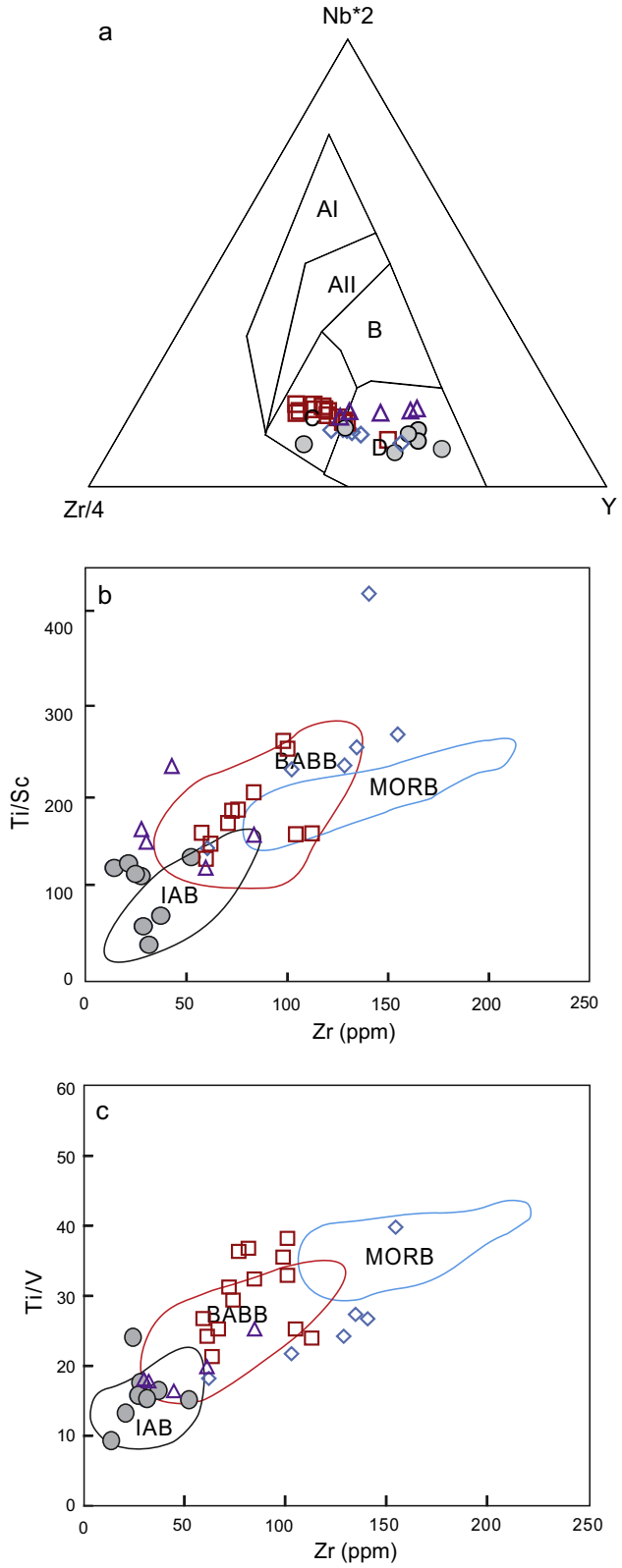

Fig. 13. Discrimination diagrams for the tectonic setting of the Wuling gabbro and its coeval mafic rocks form the Awulale Mountains: (a) Zr/4–Nb × 2–Y diagram. AI, AII: Within-Plate alkaline basalts; AII, C: Within-Plate tholeiitic basalts; B: E-MORB; C, D: Volcanic arc basalts; D: N-MORB (after Meschede (1986)), (b) Ti/Sc vs. Zr and (c) Ti/V vs. Zr (after Gribble et al. (1996)). The symbols are the same to those of Fig. 5.

The REE patterns of the Wuling gabbro and coeval mafic rocks are similar to that of the E-MORB (Fig. 6a) and the $(^{87}Sr/^{86}Sr)_i$

and $\varepsilon_{Nd}(t)$ values plot on the overlapping region of the Middle Ocean Ridge basalts and the Island Arc Volcanics, suggesting the involvement of MORB components (Fig. 10a). Such compositional signatures of the Wuling gabbro is in conformity with the geochemical affinity to both arc volcanics and MORB source, which is the characteristic features of back-arc basin basalts (BABBs) (e.g., Shinjo et al., 1999; Xu et al., 2003; Wang et al., 2007). In general, the geochemical characteristics of BABBs are either MORB-like with negligible LILE enrichment and HFSE depletion or transitional between MORB and arc magmas due to spatial relation between arc and back-arc systems (Stern et al., 1990; Gribble et al., 1996; Smith et al., 2001; Langmuir et al., 2006; Pearce and Stern, 2006; Manikyamba et al., 2009). The former type of BABBs is maintained in mature back-arc system where the domain of back-arc basin melts is spatially separated and distinguishable from subduction-arc regime (Stern et al., 1990). However, the later type is produced in nascent or initial back-arc system, and the proximity between subduction-related arc environment and back-arc basin, where the interaction between MORB-like and arc-like mantle components account for the arc-like composition of BABBs (Manikyamba et al., 2014). In the Nb–Zr–Y diagram (Fig. 13a), the Wuling gabbro and its coeval mafic rocks are ploted in the field of volcanic arc basalt and N-MORB regions. Ti, Sc, V and Zr discrimination diagrams have also been used by previous workers to discriminate between island arc basalts (IABs), BABAs and MORBs (Gamble et al., 1994; Polat et al., 1999; Manikyamba et al., 2014). The Wuling gabbro samples mainly fall within the field of IABs and near the field of BABBs on Ti/Sc and Ti/V vs. Zr diagrams (Fig. 13b and c). The affinity of the Wuling gabbro displays arc geochemical signatures is in conformity with their generation in a nascent back-arc environment proximal to an arc setting. The spots of coeval mafic rocks scatter through three fields but mostly fall in the field of BABBs (Fig. 13b and c), which may be attributed to different degrees of mixing between the arc-like component and the MORB-like component.

5.5. Tectonic model: arc–nascent back-arc

The Central Tianshan Arc is thought to have been separated from the Tarim block by the South Tianshan back-arc extension during the Late Ordovician–Early Silurian (Gao et al., 2009; Qian et al., 2009; Wang et al., 2008, 2011). As the closure of Terskey Ocean at the end of the Late Ordovician, the Central Tianshan Arc amalgamated with the Yili Block as the Yili–Central Tianshan Block (Lomize et al., 1997; Qian et al., 2009). From Early Silurian to Early Carboniferous, the South Tianshan Ocean was subducted beneath the YCTB (Gao et al., 1998; Qian et al., 2009; Long et al., 2011). The middle Silurian Jingbulake mafic–ultramafic intrusion and the late Carboniferous Luotuogou gabbro and Bulusitai gabbro from the Central Tianshan were both thought to have formed during the northward subduction of the South Tianshan Ocean (Yang and Zhou, 2009; Tang et al., 2012; Tian et al., 2014). The Sr–Nd isotopic range of these intrusions is overlapped with the Awulale Carboniferous basalt on our studied samples (Fig. 10a). The geochemical signatures of the Wuling gabbro and its coeval mafic rocks in the Awulale Mountains indicate a heterogeneous mantle source in a nascent back-arc system proximal to the arc regime. We propose that the Nalati Mountains of the Central Tianshan are spatially paired with the Awulale Mountains to constitute a late Carboniferous arc–nascent back-arc system in the western Tianshan (Fig. 14).

At ~313 Ma, an arc–nascent back-arc system was developed between the Nalati Mountains and Awulale Mountains in the western Tianshan. At a nascent back-arc environment, the back-arc center just began to rift and arc-related magmatism was still active. In the arc–nascent back-arc system, the Awulale Mountains acted as a back-arc rifting center, where decompression melting of MORB-like mantle and flux-induced partial melting of mantle wedge caused mixing between these two mantle sources. We propose that two major magma sources, a MORB-like mantle domain and a subduction component, are required for the generation of the Wuling gabbro and its coeval mafic rocks. An extensional environment is necessary for the upwelling of the deep MORB-like component and the slab roll-back might play a role in this process. Meanwhile, the fluid released from the slab enhanced decompression melting, allowing depleted mantle sources behind the arc to melt extensively. However, at the end of late Carboniferous, the South Tianshan Ocean closed and the compressional stress from the collision between the Tarim Plate and the YCTB made the Awulale back-arc center stop spreading to develop a back-arc

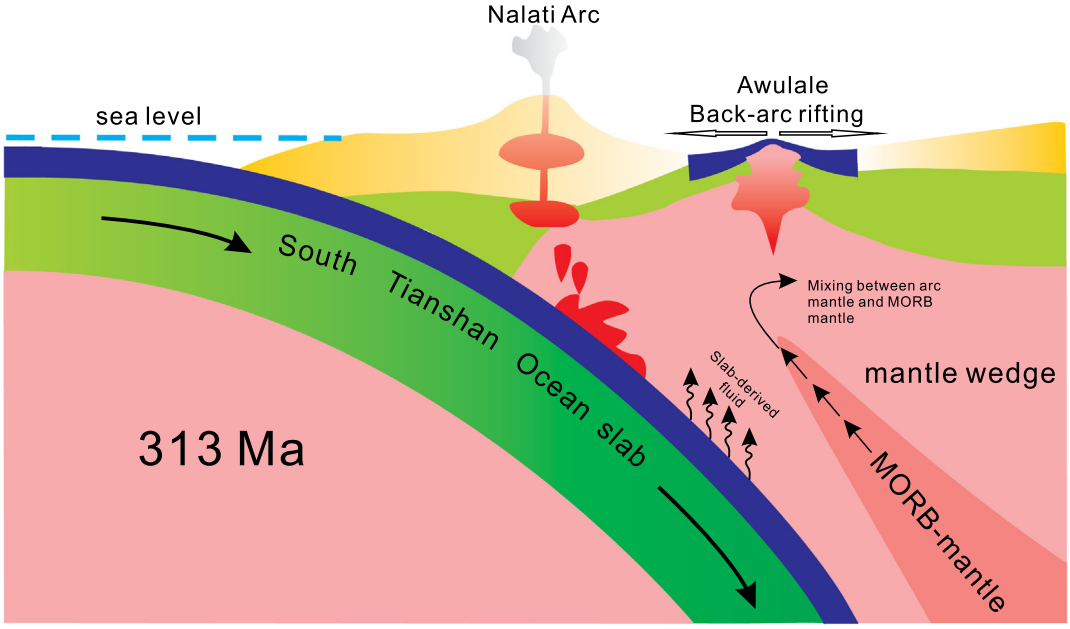

Fig. 14. Cartoon showing schematic tectonic model of an arc–nascent back-arc setting for the Wuling hornblende gabbro (modified after Manikyamba et al., 2014).

basin, which could well interpret the absence of oceanic crust in the center of the YCTB.

6. Conclusion

The Wuling (poikilitic) hornblende gabbro from the eastern Awulale Mountain was emplaced in the late Carboniferous (313 ± 3 Ma). Two stage crystallization processes are applied to interpret its mineral composition. At the early stage, clinopyroxene, anorthite and Fe-oxides were crystallized from the basaltic magma. At the late stage, hornblende and plagioclase (andesine to albite) crystallized from the evolved water-rich andesitic melt. The geochemical and mineralogical signatures of the Wuling gabbro indicate that it was generated in a subduction-related setting and the mantle wedge was fluxed by fluids released by the slab. The REE and Sr–Nd–Hf isotopic signatures of the Wuling gabbro and its coeval mafic rocks in the Awulale Mountains imply a shallow but heterogeneous mantle source with the involvement of a deep MORB-like component into the arc mantle. We propose that they were generated in a nascent back-arc environment. An arc–nascent back-arc system was developed between the Nalati Mountains and the Awulale Mountains during the late Carboniferous, where decompression melting of MORB-like mantle and partial melting of mantle wedge led to mixing between these two mantle sources. The arc-type features of them were inherited from the strong subduction inputs during the initial stage of back-arc rifting. However, thanks to the compressional stress from the collision between the Tarim Plate and the YCTB at the end of late Carboniferous, the back-arc rifting ceased.

Acknowledgments

This work was financially supported by the National Natural Science Foundation of China (U1203291, 41273056, 41373031 and the 135 project of GIGCAS (Y234131A07)). We thank Guang-Qian Hu, Xiang-Lin Tu, Jin-Long Ma, Cong-Ying Li and Le Zhang for help with analytical work and Prof. Zhen-Hua Zhao and Dr. Huang Dong for thoughtful discussions. Specially, we thanks Prof. Wen-Jiao Xiao and two anonymous reviewers for their valuable advice. This is GIGCAS contribution No. IS-2027.

Appendix A. Supplementary material

Supplementary data associated with this article can be found, in the online version, at http://dx.doi.org/10.1016/j.jseaes.2015.01.016.

References

Allen, M.B., Windley, B.F., Zhang, C., 1993. Palaeozoic collisional tectonics and magmatism of the Chinese Tien Shan, central Asia. Tectonophysics 220, 89–115.
Altherr, R., Topuz, G., Siebel, W., Sen, C., Meyer, H.P., Satir, M., Lahaye, Y., 2008. Geochemical and Sr–Nd–Pb isotopic characteristics of Paleocene plagioleucitites from the Eastern Pontides (NE Turkey). Lithos 105, 149–161.
Altunkaynak, S., Genc, S.C., 2008. Petrogenesis and time-progressive evolution of the Cenozoic continental volcanism in the Biga Peninsula, NW Anatolia (Turkey). Lithos 102, 316–340.
Arculus, R.J., Wills, K.J.A., 1980. The petrology of plutonic blocks and inclusions from the lesser Antilles Island Arc. J. Petrol. 21, 743–799.
Beard, J.S., 1986. Characteristic mineralogy of arc-related cumulate gabbros – implications for the tectonic setting of gabbroic plutons and for andesite genesis. Geology 14, 848–851.
Beard, J.S., Borgia, A., 1989. Temporal variation of mineralogy and petrology in cognate gabbroic enclaves at Arenal volcano, Costa Rica. Contrib. Miner. Petrol. 103, 110–122.
Belousova, E., Griffin, W.L., O'Reilly, S.Y., Fisher, N., 2002. Igneous zircon: trace element composition as an indicator of source rock type. Contrib. Miner. Petrol. 143, 602–622.
Black, L.P., Kamo, S.L., Allen, C.M., Aleinikoff, J.N., Davis, D.W., Korsch, R.J., Foudoulis, C., 2003. TEMORA 1: a new zircon standard for Phanerozoic U–Pb geochronology. Chem. Geol. 200, 155–170.
Blichert-Toft, J., Albarede, F., 1997. The Lu–Hf isotope geochemistry of chondrites and the evolution of the mantle-crust system. Earth Planet. Sci. Lett. 148, 343–358.
Bonev, N., Stampfli, G., 2009. Gabbro, plagiogranite and associated dykes in the supra-subduction zone Evros Ophiolites, NE Greece. Geol. Mag. 146, 72–91.
Castillo, P.R., Janney, P.E., Solidum, R.U., 1999. Petrology and geochemistry of Camiguin Island, southern Philippines: insights to the source of adakites and other lavas in a complex arc setting. Contrib. Miner. Petrol. 134, 33–51.
Charvet, J., Shu, L.S., Laurent-Charvet, S., 2007. Paleozoic structural and geodynamic evolution of eastern Tianshan (NW China): welding of the Tarim and Junggar plates. Episodes 30, 162–186.
Chen, J.F., Man, F.S., Ni, S.B., 1995. Neodymium and strontium isotopic geochemistry of mafic-ultramafic intrusions from Qinbulake rock belt, West Tianshan Mountain, Xinjiang. Geochimica 24, 121–127.
Chu, N.C., Taylor, R.N., Chavagnac, V., Nesbitt, R.W., Boella, R.M., Milton, J.A., German, C.R., Bayon, G., Burton, K., 2002. Hf isotope ratio analysis using multi-collector inductively coupled plasma mass spectrometry: an evaluation of isobaric interference corrections. J. Anal. At. Spectrom. 17, 1567–1574.
Condomines, M., Hemond, C., Allègre, C.J., 1988. U–Th–Ra radioactive disequilibria and magmatic processes. Earth Planet. Sci. Lett. 90, 243–262.
Conrad, W.K., Kay, R.W., 1984. Ultramafic and mafic inclusions from Adak Island: crystallization history, and implications for the nature of primary magmas and crustal evolution in the Aleutian Arc. J. Petrol. 25, 88–125.
Costa, F., Dungan, M., Singer, B., 2002. Hornblende-and phlogopite-bearing gabbroic xenoliths from Volcán San Pedro (36 S), Chilean Andes: evidence for melt and fluid migration and reactions in subduction-related plutons. J. Petrol. 43, 219–241.
Debari, S.M., 1994. Petrogenesis of the Fiambala Gabbroic Intrusion, Northwestern Argentina, a Deep-Crustal Syntectonic Pluton in a Continental Magmatic Arc. J. Petrol. 35, 679–713.
Debievre, P., Taylor, P.D.P., 1993. Table of the isotopic compositions of the elements. Int. J. Mass Spectrom. Ion Processes 123, 149–166.
DePaolo, D.J., 1988. Neodymium Isotope Geochemistry: An Introduction. Springer-Verlag, Berlin.
Dong, C., Xu, X., Chen, X., Zhou, X., 1997. Mineralogical record of the crystallization processes of Pingtan hornblende gabbro, Fujian. Acta Mineral. Sinica 17, 285–290.
Feng, J.X., Shi, F.P., Wang, B.Y., Hu, J.M., Wang, J.T., Tian, J.Q., 2010. Volcanogenic Iron Deposits in the Awulale Metallogenic Belt in Western Tianshan. Geological Publishing House, Beijing, pp. 16–112.
Ferry, J.M., Watson, E.B., 2007. New thermodynamic models and revised calibrations for the Ti-in-zircon and Zr-in-rutile thermometers. Contrib. Miner. Petrol. 154, 429–437.
Gamble, J., Wright, I., Woodhead, J., McCulloch, M., 1994. Arc and back-arc geochemistry in the southern Kermadec arc-Ngatoro Basin and offshore Taupo Volcanic Zone, SW Pacific. Geol. Soc., London, Special Publ. 81, 193–212.
Gao, J., Li, M.S., Xiao, X.C., Tang, Y.Q., He, G.Q., 1998. Paleozoic tectonic evolution of the Tianshan Orogen, northwestern China. Tectonophysics 287, 213–231.
Gao, J., Long, L., Klemd, R., Qian, Q., Liu, D., Xiong, X., Su, W., Liu, W., Wang, Y., Yang, F., 2009. Tectonic evolution of the South Tianshan orogen and adjacent regions, NW China: geochemical and age constraints of granitoid rocks. Int. J. Earth Sci. 98, 1221–1238.
Genc, S.C., Tuysuz, O., 2010. Tectonic setting of the Jurassic bimodal magmatism in the Sakarya Zone (Central and Western Pontides), Northern Turkey: a geochemical and isotopic approach. Lithos 118, 95–111.
Goldstein, S.L., Onions, R.K., Hamilton, P.J., 1984. A Sm–Nd isotopic study of atmospheric dusts and particulates from major river systems. Earth Planet. Sci. Lett. 70, 221–236.
Gribble, R.F., Stern, R.J., Bloomer, S.H., Stüben, D., O'Hearn, T., Newman, S., 1996. MORB mantle and subduction components interact to generate basalts in the southern Mariana Trough back-arc basin. Geochim. Cosmochim. Acta 60, 2153–2166.
Griffin, W.L., Pearson, N.J., Belousova, E., Jackson, S.E., van Achterbergh, E., O'Reilly, S.Y., Shee, S.R., 2000. The Hf isotope composition of cratonic mantle: LAM–MC–ICPMS analysis of zircon megacrysts in kimberlites. Geochim. Cosmochim. Acta 64, 133–147.
Griffin, W.L., Wang, X., Jackson, S.E., Pearson, N.J., O'Reilly, S.Y., Xu, X.S., Zhou, X.M., 2002. Zircon chemistry and magma mixing, SE China: In-situ analysis of Hf isotopes, Tonglu and Pingtan igneous complexes. Lithos 61, 237–269.
Han, B.F., Guo, Z.J., Zhang, Z.C., Zhang, L., Chen, J.F., Song, B., 2010. Age, geochemistry, and tectonic implications of a late Paleozoic stitching pluton in the North Tian Shan suture zone, western China. Geol. Soc. Am. Bull. 122, 627–640.
Han, B.-F., He, G.-Q., Wang, X.-C., Guo, Z.-J., 2011. Late Carboniferous collision between the Tarim and Kazakhstan-Yili terranes in the western segment of the South Tian Shan Orogen, Central Asia, and implications for the Northern Xinjiang, western China. Earth Sci. Rev. 109, 74–93.
Harris, A.C., Allen, C.M., Bryan, S.E., Campbell, I.H., Holcombe, R.J., Palin, J.M., 2004. ELA–ICP–MS U–Pb zircon geochronology of regional volcanism hosting the Bajo de la Alumbrera Cu–Au deposit: implications for porphyry-related mineralization. Miner. Deposita 39, 46–67.
Hart, S., Gerlach, D., White, W., 1986. A possible new Sr–Nd–Pb mantle array and consequences for mantle mixing. Geochim. Cosmochim. Acta 50, 1551–1557.

Hart, S., Hauri, E., Oschmann, L., Whitehead, J., 1992. Mantle plumes and entrainment: isotopic evidence. Science 256, 517.
Hawkesworth, C.J., Gallagher, K., Hergt, J.M., Mcdermott, F., 1993. Mantle and slab contributions in arc magmas. Annu. Rev. Earth Planet. Sci. 21, 175–204.
Hawkesworth, C.J., Turner, S.P., McDermott, F., Peate, D.W., vanCalsteren, P., 1997. U–Th isotopes in arc magmas: implications for element transfer from the subducted crust. Science 276, 551–555.
Hegner, E., Klemd, R., Kröner, A., Corsini, M., Alexeiev, D.V., Iaccheri, L.M., Zack, T., Dulski, P., Xia, X., Windley, B.F., 2010. Mineral ages and P–T conditions of Late Paleozoic high-pressure eclogite and provenance of mélange sediments from Atbashi in the south Tianshan orogen of Kyrgyzstan. Am. J. Sci. 310, 916–950.
Hickeyvargas, R., Abdollahi, M.J., Parada, M.A., Lopezescobar, L., Frey, F.A., 1995. Crustal Xenoliths from Calbuco Volcano, Andean Southern Volcanic Zone – implications for crustal composition and magma-crust interaction. Contrib. Miner. Petrol. 119, 331–344.
Hong, D.W., Wang, S.G., Xie, X.L., Zhang, J.S., Wang, T., 2003. Metallogenic province derived from mantle sources: Nd, Sr, S and Pb isotope evidence from the Central Asian Orogenic Belt. Gondwana Res. 6, 711–728.
Hu, A., Jahn, B.-M., Zhang, G., Chen, Y., Zhang, Q., 2000. Crustal evolution and Phanerozoic crustal growth in northern Xinjiang: Nd isotopic evidence. Part I. Isotopic characterization of basement rocks. Tectonophysics 328, 15–51.
Humphris, S.E., 1984. The mobility of the rare earth elements in the crust. In: Henderson, P. (Ed.), Rare Earth Element Geochemistry. Elsevier, Amsterdam, pp. 317–342.
Irvine, T.N., Baragar, W.R.A., 1971. A guide to the chemical classification of the common volcanic rocks. Can. J. Earth Sci. 8, 523–548.
Irving, A.J., Frey, F.A., 1978. Distribution of trace elements between garnet megacrysts and host volcanic liquids of kimberlitic to rhyolitic composition. Geochim. Cosmochim. Acta 42, 771–787.
Jacobsen, S.B., Wasserburg, G.J., 1980. Sm–Nd isotopic evolution of chondrites. Earth Planet. Sci. Lett. 50, 139–155.
Jahn, B.-M., 2004. The Central Asian Orogenic Belt and growth of the continental crust in the Phanerozoic. Geol. Soc., London, Special Publ. 226, 73–100.
Jiang, Y.-H., Jiang, S.-Y., Dai, B.-Z., Liao, S.-Y., Zhao, K.-D., Ling, H.-F., 2009. Middle to late Jurassic felsic and mafic magmatism in southern Hunan province, southeast China: implications for a continental arc to rifting. Lithos 107, 185–204.
Jiang, Z.S., Zhang, Z.H., Wang, Z.H., Duan, S.G., Li, F.M., Tian, J.Q., 2014. Geology, geochemistry, and geochronology of the Zhibo iron deposit in the Western Tianshan, NW China: constraints on metallogenesis and tectonic setting. Ore Geol. Rev. 57, 406–424.
Johnson, M.C., Plank, T., 2000. Dehydration and melting experiments constrain the fate of subducted sediments. Geochem. Geophys. Geosyst. 1, 1007.
Jung, C., Jung, S., Hoffer, E., Berndt, J., 2006. Petrogenesis of Tertiary mafic alkaline magmas in the Hocheifel, Germany. J. Petrol. 47, 1637–1671.
Kelemen, P., Hanghøj, K., Greene, A., 2003. One view of the geochemistry of subduction-related magmatic arcs, with an emphasis on primitive andesite and lower crust. Treatise Geochem. 3, 593–659.
Keskin, M., 2005. Domal Uplift and Volcanism in a Collision Zone without a Mantle Plume: Evidence from Eastern Anatolia. <http://www.mantleplumes.org/Anatolia.html>.
Labanieh, S., Chauvel, C., Germa, A., Quidelleur, X., 2012. Martinique: a clear case for sediment melting and slab dehydration as a function of distance to the trench. J. Petrol. 53, 2441–2464.
Langmuir, C., Bézos, A., Escrig, S., Parman, S., 2006. Chemical systematics and hydrous melting of the mantle in back-arc basins. Back-Arc Spreading Syst. Geol., Biol., Chem., Phys. Interact., 87–146
Lee, C.-T.A., Luffi, P., Plank, T., Dalton, H., Leeman, W.P., 2009. Constraints on the depths and temperatures of basaltic magma generation on Earth and other terrestrial planets using new thermobarometers for mafic magmas. Earth Planet. Sci. Lett. 279, 20–33.
Li, X.-H., 1997. Geochemistry of the Longsheng Ophiolite from the southern margin of Yangtze Craton, SE China. Geochem. J. Jpn. 31, 323–338.
Li, X.H., Qi, C.S., Liu, Y., Liang, X.R., Tu, X.L., Xie, L.W., Yang, Y.H., 2005. Petrogenesis of the Neoproterozoic bimodal volcanic rocks along the western margin of the Yangtze Block: new constraints from Hf isotopes and Fe/Mn ratios. Chin. Sci. Bull. 50, 2481–2486.
Li, Y.J., Li, Z.C., Zhou, J.B., Gao, Z.H., Gao, Y.L., Tong, L.M., Liu, J., 2009a. Division of the Carboniferous lithostratigraphic units in Awulale area, western Tianshan. Acta Petrol. Sinica 25, 1332–1340.
Li, Y.J., Gao, Y.L., Tong, L.L., Guo, W.J., Tong, L.M., 2009b. Tempestite of Akeshake Formation in Awulale Area, Western Tianshan and its significance. Earth Sci. Front. 16, 341–348.
Li, X.H., Long, W.G., Li, Q.L., Liu, Y., Zheng, Y.F., Yang, Y.H., Chamberlain, K.R., Wan, D.F., Guo, C.H., Wang, X.C., Tao, H., 2010a. Penglai zircon megacrysts: a potential new working reference material for microbeam determination of Hf–O isotopes and U–Pb age. Geostand. Geoanal. Res. 34, 117–134.
Li, X.-P., Zhang, L.-F., Wilde, S.A., Song, B., Liu, X.-M., 2010b. Zircons from rodingite in the Western Tianshan serpentinite complex: mineral chemistry and U–Pb ages define nature and timing of rodingitization. Lithos 118, 17–34.
Li, H., Ling, M.-X., Li, C.-Y., Zhang, H., Ding, X., Yang, X.-Y., Fan, W.-M., Li, Y.-L., Sun, W.-D., 2012. A-type granite belts of two chemical subgroups in central eastern China: indication of ridge subduction. Lithos 150, 26–36.
Li, N.-B., Niu, H.-C., Shan, Q., Yang, W.-B., 2015a. Two episodes of Late Paleozoic A-type magmatism in the Qunjisayi area, western Tianshan: Petrogenesis and tectonic implications. J Asian Earth Sci. http://dx.doi.org/10.1016/j.jseaes.2014.12.015, accepted for publication.
Li, N.-B., Niu, H.-C., Zhang, X.-C., Zeng, Q.-S., Shan, Q., Li, C.-Y., Yan, S., Yang, W., 2015b. Age, petrogenesis and tectonic significance of the Fe-rich basalt in the Chagangnuoer large iron deposit, western Tianshan. Int. Geol. Rev. http://dx.doi.org/10.1080/00206814.2015.1004136, accepted for publication.
Liang, X.R., Wei, G.J., Li, X.H., Liu, Y., 2003. Precise measurement of $^{143}Nd/^{144}Nd$ and Sm/Nd ratios using multiple-collectors inductively coupled plasma-mass spectrometer (MC-ICPMS). Geochimica 32, 91–96.
Liang, H.Y., Campbell, I.H., Allen, C., Sun, W.D., Liu, C.Q., Yu, H.X., Xie, Y.W., Zhang, Y.Q., 2006. Zircon Ce4+/Ce3+ ratios and ages for Yulong ore-bearing porphyries in eastern Tibet. Miner. Deposita 41, 152–159.
Liu, Y.S., Gao, S., Hu, Z.C., Gao, C.G., Zong, K.Q., Wang, D.B., 2010a. Continental and Oceanic crust recycling-induced melt-peridotite interactions in the trans-North China Orogen: U–Pb dating, Hf isotopes and trace elements in zircon from Mantle Xenoliths. J. Petrol. 51, 537–571.
Liu, Y.S., Hu, Z.C., Zong, K.Q., Gao, C.G., Gao, S., Xu, J.A., Chen, H.H., 2010b. Reappraisement and refinement of zircon U–Pb isotope and trace element analyses by LA–ICP–MS. Chin. Sci. Bull. 55, 1535–1546.
Liu, X., Qian, Q., Su, W., Li, J., 2012. Pluton from Muhanbasitao in the western of Awulale, Western Tianshan: geochemistry, geochronology and geological implications. Acta Petrol. Sin. 28, 2401–2413.
Liu, H., Wang, B., Shu, L., Jahn, B.-M., Lizuka, Y., 2014. Detrital zircon ages of Proterozoic meta-sedimentary rocks and Paleozoic sedimentary cover of the northern Yili Block: implications for the tectonics of microcontinents in the Central Asian Orogenic Belt. Precambr. Res. 252, 209–222.
Lomize, M.G., Demina, L.I., Zarshchicov, A.V., 1997. The Kyrgyz–Terskei paleoceanic basin in the Tien Shan. Geotectonics 31, 463–482 (in Russian with English abstract).
Long, L.L., Gao, J., Klemd, R., Beier, C., Qian, Q., Zhang, X., Wang, J.B., Jiang, T., 2011. Geochemical and geochronological studies of granitoid rocks from the Western Tianshan Orogen: implications for continental growth in the southwestern Central Asian Orogenic Belt. Lithos 126, 321–340.
Luan, X.D., Zhang, B.R., Gao, Y.L., Yang, J.Q., Li, Y.J., 2008. New materials of stratigraphic classification and correlation of the carboniferous in Awulale area, Western Tianshan. Xinjiang Geol. 26, 231–235.
Ludwig, K., 2008. Isoplot 3.6; a Geochronology Toolkit for Microsoft Excel. Berkeley Geochronology Center, 77p.
Ma, L., Wang, Q., Wyman, D.A., Jiang, Z.-Q., Yang, J.-H., Li, Q.-L., Gou, G.-N., Guo, H.-F., 2013. Late Cretaceous crustal growth in the Gangdese area, southern Tibet: Petrological and Sr–Nd–Hf–O isotopic evidence from Zhengga diorite–gabbro. Chem. Geol. 349–350, 54–70.
Maitre, R.W.L., Bateman, P., Dudek, A., Keller, J., Lemeyre, J., Bas, M.J.L., Sabine, P.A., Schmid, R., Sorensen, H., Streckeisen, A., Wooley, A.R., Zanettin, B., 1989. A Classification of Igneous Rocks and Glossary of Terms. Blackwell, Oxford.
Mandal, A., Ray, A., Debnath, M., Paul, S.P., 2012. Petrology, geochemistry of hornblende gabbro and associated dolerite dyke of Paharpur, Puruliya, West Bengal: implication for petrogenetic process and tectonic setting. J. Earth Syst. Sci. 121, 793–812.
Manikyamba, C., Kerrich, R., Khanna, T.C., Satyanarayanan, M., Krishna, A.K., 2009. Enriched and depleted arc basalts, with Mg-andesites and adakites: a potential paired arc–back-arc of the 2.6 Ga Hutti greenstone terrane, India. Geochim. Cosmochim. Acta 73, 1711–1736.
Manikyamba, C., Ganguly, S., Santosh, M., Singh, M.R., Saha, A., 2014. Arc-nascent back-arc signature in metabasalts from the Neoarchaean Jonnagiri greenstone terrane, Eastern Dharwar Craton, India. Geol. J. n/a–n/a.
Mcculloch, M.T., Black, L.P., 1984. Sm–Nd isotopic systematics of ender by land granulites and evidence for the redistribution of Sm and Nd during metamorphism. Earth Planet. Sci. Lett. 71, 46–58.
Meschede, M., 1986. A method of discriminating between different types of mid-ocean ridge basalts and continental tholeiites with the Nb–Zr–Y diagram. Chem. Geol. 56, 207–218.
Metcalf, R.V., Shervais, J.W., 2008. Suprasubduction-zone ophiolites: is there really an ophiolite conundrum? Geol. Soc. Am. Special Papers 438, 191–222.
Munteanu, M., Wilson, A., Yao, Y., Harris, C., Chunnett, G., Luo, Y., 2010. The Tongde dioritic pluton (Sichuan, SW China) and its geotectonic setting: regional implications of a local-scale study. Gondwana Res. 18, 455–465.
Niu, H.C., Shan, Q., Yang, W.B., Luo, Y., Li, N.B., Yu, X.Y., 2011. The discovery of Fe-rich basalt–Rhyolite association in the Chagangnuoer area, westernTianshan, Xinjiang (Abstract). Bull. Mineral., Petrol., Geochem. 30, 85.
Niu, H.C., Luo, Y., Li, N.B., Jiang, Y.H., Yang, W.B., Shan, Q., Yu, X.Y., 2012. Study on the Cu-mineralization of the Chagangnuoer Fe-deposit in the Awulale area, Xinjiang. J. Nanjing Univ. (Natl. Sci.) 48, 256–265.
Panjasawatwong, Y., Danyushevsky, L.V., Crawford, A.J., Harris, K.L., 1995. An experimental-study of the effects of melt composition on plagioclase – melt equilibria at 5-Kbar and 10-Kbar – implications for the origin of magmatic high-an plagioclase. Contrib. Miner. Petrol. 118, 420–432.
Pearce, J.A., 2008. Geochemical fingerprinting of oceanic basalts with applications to ophiolite classification and the search for Archean oceanic crust. Lithos 100, 14–48.
Pearce, J.A., Peate, D.W., 1995. Tectonic implications of the composition of volcanic arc magmas. Ann. Rev. Earth Planet. Sci. 23, 251–286.
Pearce, J.A., Stern, R.J., 2006. Origin of back-arc basin magmas: trace element and isotope perspectives. Back-Arc Spreading Syst.: Geol., Biol., Chem., Phys. Interact., 63–86
Pearce, N.J.G., Perkins, W.T., Westgate, J.A., Gorton, M.P., Jackson, S.E., Neal, C.R., Chenery, S.P., 1997. A compilation of new and published major and trace

element data for NIST SRM 610 and NIST SRM 612 glass reference materials. Geostandards Newslett. –J. Geostandards Geoanalysis 21, 115–144.
Peccerillo, A., Taylor, S.R., 1976. Geochemistry of Eocene calc-alkaline volcanic rocks from the Kastamonu area, northern Turkey. Contrib. Miner. Petrol. 58, 63–81.
Perfit, M., Gust, D., Bence, A.E., Arculus, R., Taylor, S., 1980. Chemical characteristics of island-arc basalts: implications for mantle sources. Chem. Geol. 30, 227–256.
Pin, C., Duthou, J.L., 1990. Sources of Hercynian Granitoids from the French Massif-Central – inferences from Nd isotopes and consequences for crustal evolution. Chem. Geol. 83, 281–296.
Plank, T., 2005. Constraints from thorium/lanthanum on sediment recycling at subduction zones and the evolution of the continents. J. Petrol. 46, 921–944.
Polat, A., Hofmann, A.W., 2003. Alteration and geochemical patterns in the 3.7–3.8 Ga Isua greenstone belt, West Greenland. Precambr. Res. 126, 197–218.
Polat, A., Kerrich, R., Wyman, D.A., 1999. Geochemical diversity in oceanic komatiites and basalts from the late Archean Wawa greenstone belts, Superior Province, Canada: trace element and Nd isotope evidence for a heterogeneous mantle. Precambr. Res. 94, 139–173.
Polat, A., Hofmann, A.W., Rosing, M.T., 2002. Boninite-like volcanic rocks in the 3.7–3.8 Ga Isua greenstone belt, West Greenland: geochemical evidence for intra-oceanic subduction zone processes in the early Earth. Chem. Geol. 184, 231–254.
Price, R.C., Gray, C.M., Wilson, R.E., Frey, F.A., Taylor, S.R., 1991. The effects of weathering on rare-earth element, Y and Ba abundances in Tertiary basalts from southeastern Australia. Chem. Geol. 93, 245–265.
Prouteau, G., Scaillet, B., Pichavant, M., Maury, R., 2001. Evidence for mantle metasomatism by hydrous silicic melts derived from subducted oceanic crust. Nature 410, 197–200.
Qian, Q., Gao, J., Klemd, R., He, G., Song, B., Liu, D., Xu, R., 2009. Early Paleozoic tectonic evolution of the Chinese South Tianshan Orogen: constraints from SHRIMP zircon U–Pb geochronology and geochemistry of basaltic and dioritic rocks from Xiate, NW China. Int. J. Earth Sci. 98, 551–569.
Richards, J.P., Kerrich, R., 2007. Special paper: adakite-like rocks: their diverse origins and questionable role in metallogenesis. Econ. Geol. 102, 537–576.
Rogers, N., Macdonald, R., Fitton, J.G., George, R., Smith, M., Barreiro, B., 2000. Two mantle plumes beneath the east African rift system: Sr, Nd and Pb isotope evidence from Kenya Rift basalts. Earth Planet. Sci. Lett. 176, 387–400.
Rollinson, H.R., 1993. Using Geochemical Data: Evaluation, Presentation, Interpretation. Longman Group UK Ltd., 352.
Rudnick, R.L., Fountain, D.M., 1995. Nature and composition of the continental crust – a lower crustal perspective. Rev. Geophys. 33, 267–309.
Said, N., Kerrich, R., 2010. Magnesian dyke suites of the 2.7 Ga Kambalda Sequence, Western Australia: evidence for coeval melting of plume asthenosphere and metasomatised lithospheric mantle. Precambr. Res. 180, 183–203.
Scherer, E.E., Cameron, K.L., Blichert-Toft, J., 2000. Lu–Hf garnet geochronology: closure temperature relative to the Sm–Nd system and the effects of trace mineral inclusions. Geochim. Cosmochim. Acta 64, 3413–3432.
Sengor, A.M.C., Natalin, B.A., Burtman, V.S., 1993. Evolution of the altaid tectonic collage and paleozoic crustal growth in Eurasia. Nature 364, 299–307.
Shinjo, R., Chung, S.L., Kato, Y., Kimura, M., 1999. Geochemical and Sr–Nd isotopic characteristics of volcanic rocks from the Okinawa Trough and Ryukyu Arc: implications for the evolution of a young, intracontinental back arc basin. J. Geophys. Res.-Solid Earth 104, 10591–10608.
Sisson, T.W., Grove, T.L., 1993. Experimental investigations of the role of H2O in calc-alkaline differentiation and subduction zone magmatism. Contrib. Miner. Petrol. 113, 143–166.
Sisson, T.W., Grove, T.L., Coleman, D.S., 1996. Hornblende gabbro sill complex at Onion Valley, California, and a mixing origin for the Sierra Nevada batholith. Contrib. Miner. Petrol. 126, 81–108.
Slama, J., Kosler, J., Condon, D.J., Crowley, J.L., Gerdes, A., Hanchar, J.M., Horstwood, M.S.A., Morris, G.A., Nasdala, L., Norberg, N., Schaltegger, U., Schoene, B., Tubrett, M.N., Whitehouse, M.J., 2008. Plesovice zircon – a new natural reference material for U–Pb and Hf isotopic microanalysis. Chem. Geol. 249, 1–35.
Smith, T.E., Huang, C.H., Walawender, M.J., Cheung, P., Wheeler, C., 1983. The gabbroic rocks of the Peninsular Ranges batholith, southern California: cumulate rocks associated with calc-alkalic basalts and andesites. J. Volcanol. Geoth. Res. 18, 249–278.
Smith, G.P., Wiens, D.A., Fischer, K.M., Dorman, L.M., Webb, S.C., Hildebrand, J.A., 2001. A complex pattern of mantle flow in the Lau backarc. Science 292, 713–716.
Stern, R.J., Lin, P.-N., Morris, J.D., Jackson, M.C., Fryer, P., Bloomer, S.H., Ito, E., 1990. Enriched back-arc basin basalts from the northern Mariana Trough: implications for the magmatic evolution of back-arc basins. Earth Planet. Sci. Lett. 100, 210–225.
Su, W., Gao, J., Klemd, R., Li, J.-L., Zhang, X., Li, X.-H., Chen, N.-S., Zhang, L., 2010. U–Pb zircon geochronology of Tianshan eclogites in NW China: implication for the collision between the Yili and Tarim blocks of the southwestern Altaids. Eur. J. Mineral. 22, 473–478.
Sun, S.-S., McDonough, W.F., 1989. Chemical and isotopic systematics of oceanic basalts: implications for mantle composition and processes. Geol. Soc. London, Special Publ. 42, 313–345.
Sun, W.D., Hu, Y.H., Kamenetsky, V.S., Eggins, S.M., Chen, M., Arculus, R.J., 2008. Constancy of Nb/U in the mantle revisited. Geochim. Cosmochim. Acta 72, 3542–3549.
Tang, G.-J., Wang, Q., Wyman, D.A., Li, Z.-X., Xu, Y.-G., Zhao, Z.-H., 2012. Metasomatized lithosphere–asthenosphere interaction during slab roll-back: evidence from Late Carboniferous gabbros in the Luotuogou area, Central Tianshan. Lithos 155, 67–80.
Tang, G.-J., Chung, S.-L., Wang, Q., Wyman, D.A., Dan, W., Chen, H.-Y., Zhao, Z.-H., 2014. Petrogenesis of a Late Carboniferous mafic dike–granitoid association in the western Tianshan: response to the geodynamics of oceanic subduction. Lithos 202–203, 85–99.
Tatsumi, Y., Eggins, S.M., 1995. Subduction Zone Magmatism. Blackwell, Cambridge, 211 pp.
Tian, Y.Z., Yang, J.S., Liu, F., Zhao, Y.J., Feng, G.Y., Niu, X.L., Zhang, L., Gao, J., 2014. Petrological characteristics of Bulusitai gabbro and its constraint to the time of South Tianshan ocean subduction. Acta Petrol. Sin. 30, 2363–2380.
Ulmer, P., Callegari, E., Sonderegger, U.C., 1983. Genesis of the mafic and ultramafic rocks and their genetical relations to the tonalitic–trondhjemitic granitoids of the southern part of the Adamello batholith (Northern Italy). Mem. Soc. Geol. Ital. 26, 171–222.
Wan, B., Xiao, W., Windley, B.F., Yuan, C., 2013. Permian hornblende gabbros in the Chinese Altai from a subduction-related hydrous parent magma, not from the Tarim mantle plume. Lithosphere 5, 290–299.
Wang, J., Xu, X., 2006. Post-collisional tectonic evolution and metallogenesis in northern Xinjiang, China. Acta Geol. Sin. 80, 23–31.
Wang, Y.J., Zhao, G.C., Fan, W.M., Peng, T.P., Sun, L.H., Xia, X.P., 2007. LA–ICP–MS U–Pb zircon geochronology and geochemistry of Paleoproterozoic mafic dykes from western Shandong Province. implications for back-arc basin magmatism in the Eastern Block, North China Craton. Precambr. Res. 154, 107–124.
Wang, B., Faure, M., Shu, L.S., Cluzel, D., Charvet, J., De Jong, K., Chen, Y., 2008. Paleozoic tectonic evolution of the Yili Block, western Chinese Tianshan. Bull. Soc. Geol. Fr. 179, 483–490.
Wang, B., Faure, M., Shu, L.S., de Jong, K., Charvet, J., Cluzel, D., Jahn, B.M., Chen, Y., Ruffet, G., 2010. Structural and geochronological study of High-Pressure metamorphic rocks in the Kekesu section (Northwestern China): implications for the late Paleozoic tectonics of the southern Tainshan. J. Geol. 118, 59–77.
Wang, B., Shu, L.S., Faure, M., Jahn, B.-M., Cluzel, D., Charvet, J., Chung, S.-L., Meffre, S., 2011. Paleozoic tectonics of the southern Chinese Tianshan: insights from structural, chronological and geochemical studies of the Heiyingshan ophiolitic mélange (NW China). Tectonophysics 497, 85–104.
Wang, B., Liu, H., Shu, L., Jahn, B.-M., Chung, S.-L., Zhai, Y., Liu, D., 2014a. Early Neoproterozoic crustal evolution in northern Yili Block: insights from migmatite, orthogneiss and leucogranite of the Wenquan metamorphic complex in the NW Chinese Tianshan. Precambr. Res. 242, 58–81.
Wang, B., Shu, L., Liu, H., Gong, H., Ma, Y., Mu, L., Zhong, L., 2014b. First evidence for ca. 780 Ma intra-plate magmatism and its implications for Neoproterozoic rifting of the North Yili Block and tectonic origin of the continental blocks in SW of Central Asia. Precambr. Res.
Watson, E.B., 1982. Basalt contamination by continental-crust–some experiments and models. Contrib. Mineral. Petrol. 80, 73–87.
Watson, E.B., Wark, D.A., Thomas, J.B., 2006. Crystallization thermometers for zircon and rutile. Contrib. Mineral. Petrol. 151, 413–433.
Wei, G.J., Liang, X.R., Li, X.H., Liu, Y., 2002. Precise measurement of Sr isotopic composition of liquid and solid base using (LP) MC-ICPMS. Geochimica 31, 295–305.
Winchester, J.A., Floyd, P.A., 1977. Geochemical discrimination of different magma series and their differentiation products using immobile elements. Chem. Geol. 20, 325–343.
Windley, B.F., Allen, M.B., Zhang, C., Zhao, Z.-Y., Wang, G.-R., 1990. Paleozoic accretion and Cenozoic redeformation of the Chinese Tien Shan Range, central Asia. Geology 18, 128–131.
Woodhead, J.D., Eggins, S.M., Johnson, R.W., 1998. Magma genesis in the New Britain Island Arc: further insights into melting and mass transfer processes. J. Petrol. 39, 1641–1668.
Woodhead, J.D., Hergt, J.M., Davidson, J.P., Eggins, S.M., 2001. Hafnium isotope evidence for 'conservative' element mobility during subduction zone processes. Earth Planet. Sci. Lett. 192, 331–346.
Wu, F.Y., Yang, Y.H., Xie, L.W., Yang, J.H., Xu, P., 2006. Hf isotopic compositions of the standard zircon and baddeleyites used in U–Pb geochronology. Chem. Geol. 234, 105–126.
Xia, L.Q., Xia, Z.C., Xu, X.Y., Li, X.M., Ma, Z.P., Wang, L.S., 2004a. Carboniferous Tianshan igneous megaprovince and mantle plume [J]. Reg. Geol. China Z 2.
Xia, L.-Q., Xu, X.-Y., Xia, Z.-C., Li, X.-M., Ma, Z.-P., Wang, L.-S., 2004b. Petrogenesis of Carboniferous rift-related volcanic rocks in the Tianshan, northwestern China. Geol. Soc. Am. Bull. 116, 419–433.
Xia, L.-Q., Xia, Z.-C., Xu, X.-Y., Li, X.-M., Ma, Z.-P., 2008. Relative contributions of crust and mantle to the generation of the Tianshan Carboniferous rift-related basic lavas, northwestern China. J. Asian Earth Sci. 31, 357–378.
Xiao, W.J., Kusky, T., 2009. Geodynamic processes and metallogenesis of the Central Asian and related orogenic belts: Introduction. Gondwana Res. 16, 167–169.
Xiao, W.J., Windley, B.F., Badarch, G., Sun, S., Li, J., Qin, K., Wang, Z., 2004. Palaeozoic accretionary and convergent tectonics of the southern Altaids: implications for the growth of Central Asia. J. Geol. Soc. 161, 339–342.
Xiao, W., Han, C., Yuan, C., Sun, M., Lin, S., Chen, H., Li, Z., Li, J., Sun, S., 2008. Middle Cambrian to Permian subduction-related accretionary orogenesis of Northern Xinjiang, NW China: implications for the tectonic evolution of central Asia. J. Asian Earth Sci. 32, 102–117.
Xiao, W.J., Huang, B.C., Han, C.M., Sun, S., Li, J.L., 2010. A review of the western part of the Altaids: a key to understanding the architecture of accretionary orogens. Gondwana Res. 18, 253–273.

Xiao, W.J., Windley, B.F., Allen, M.B., Han, C.M., 2013. Paleozoic multiple accretionary and collisional tectonics of the Chinese Tianshan orogenic collage. Gondwana Res. 23, 1316–1341.

Xiong, X.L., Zhao, Z.H., Bai, Z.H., Mei, H.J., Xu, J.F., Wang, Q., 2001. Origin of Awulale adakitic sodium-rich rocks in western Tianshan: constraints for Nd and Sr isotopic compositions. Acta Petrol. Sin. 17, 514–522.

Xu, J.F., Castillo, P.R., Chen, F.R., Niu, H.C., Yu, X.Y., Zhen, Z.P., 2003. Geochemistry of late Paleozoic mafic igneous rocks from the Kuerti area, Xinjiang, northwest China: implications for backarc mantle evolution. Chem. Geol. 193, 137–154.

Xu, Y.-G., Lan, J.-B., Yang, Q.-J., Huang, X.-L., Qiu, H.-N., 2008. Eocene break-off of the Neo-Tethyan slab as inferred from intraplate-type mafic dykes in the Gaoligong orogenic belt, eastern Tibet. Chem. Geol. 255, 439–453.

Xue, Y.X., Zhu, Y.F., 2009. Zircon SHRIMP chronology and geochemistry of the Haladala gabbro in south-western Tianshan Mountains. Acta Petrol. Sin. 25, 1353–1363.

Yan, S., Niu, H.C., 2014. Petrography and Geochemistry of the Wuling Amphibole Gabbro and Its Implication for Iron OreMetallization. Acta Geologica Sinica (English Edition) 88 (supp. 2), 397–398.

Yan, Y.H., Xue, C.J., Zhang, Z.C., Ding, Z.X., Yang, W.H., Han, Z.H., 2013. Geochemistry and genesis of the Qunjisayi granite porphyry in the west of Awulale area, Western Tianshan Mountains. Acta Petrol. Mineral. 32, 139–153.

Yang, S.-H., Zhou, M.-F., 2009. Geochemistry of the ~430-Ma Jingbulake mafic–ultramafic intrusion in Western Xinjiang, NW China: implications for subduction related magmatism in the South Tianshan orogenic belt. Lithos 113, 259–273.

Yang, J.-H., Sun, J.-F., Chen, F., Wilde, S.A., Wu, F.-Y., 2007. Sources and petrogenesis of Late Triassic dolerite dikes in the Liaodong peninsula: implications for post-collisional lithosphere thinning of the Eastern North China craton. J. Petrol. 48, 1973–1997.

Yang, W.-B., Niu, H.-C., Shan, Q., Luo, Y., Sun, W.-D., Li, C.-Y., Li, N.-B., Yu, X.-Y., 2012. Late Paleozoic calc-alkaline to shoshonitic magmatism and its geodynamic implications, Yuximolegai area, western Tianshan, Xinjiang. Gondwana Res. 22, 325–340.

Yang, W.-B., Niu, H.-C., Shan, Q., Chen, H.-Y., Hollings, P., Li, N.-B., Yan, S., Zartman, R.E., 2014a. Geochemistry of primary-carbonate bearing K-rich igneous rocks in the Awulale Mountains, western Tianshan: implications for carbon-recycling in subduction zone. Geochim. Cosmochim. Acta 143, 143–164.

Yang, W.B., Niu, H.C., Shan, Q., Sun, W.D., Zhang, H., Li, N.B., Jiang, Y.H., Yu, X.A., 2014b. Geochemistry of magmatic and hydrothermal zircon from the highly evolved Baerzhe alkaline granite: implications for Zr–REE–Nb mineralization. Miner. Deposita 49, 451–470.

Zhang, M., O'Reilly, S.Y., 1997. Multiple sources for basaltic rocks from Dubbo, eastern Australia: geochemical evidence for plume—lithospheric mantle interaction. Chem. Geol. 136, 33–54.

Zhang, L., Ai, Y., Li, X., Rubatto, D., Song, B., Williams, S., Song, S., Ellis, D., Liou, J., 2007a. Triassic collision of western Tianshan orogenic belt, China: evidence from SHRIMP U–Pb dating of zircon from HP/UHP eclogitic rocks. Lithos 96, 266–280.

Zhang, S.-H., Liu, S.-W., Zhao, Y., Yang, J.-H., Song, B., Liu, X.-M., 2007b. The 1.75–1.68 Ga anorthosite-mangerite-alkali granitoid-rapakivi granite suite from the northern North China Craton: magmatism related to a Paleoproterozoic orogen. Precambr. Res. 155, 287–312.

Zhang, X., Tian, J.Q., Gao, J., Klemd, R., Dong, L.H., Fan, J.J., Jiang, T., Hu, C.J., Qian, Q., 2012. Geochronology and geochemistry of granitoid rocks from the Zhibo syngenetic volcano genic iron ore deposit in the Western Tianshan Mountains (NW-China): constraints on the age o f mineralization and tectonic setting. Gondwana Res. 22, 585–596.

Zhang, Z.H., Hong, W., Jiang, Z.S., Duan, S.G., Li, F.M., Shi, F.P., 2014. Geological characteristics and metallogenesis of iron deposits in western Tianshan, China. Ore Geol. Rev. 57, 425–440.

Zhao, Z.H., Bai, Z.H., Rui, Z.Y., Xiong, X.L., Mei, H.J., Wang, L.S., Wang, Y.X., Bao, Z.W., 2000. Forecasting map of igneous rocks and mineralization in northern Western Tianshan. Project reports of "Late Paleozoic volcanisms, shallow intrusive magmatism and Cu–Au polymetallic mineralization studies in northern West Tianshan" (In Chinese).

Zhao, Z.H., Guo, Z.J., Han, B.F., Wang, Y., 2006. The geochemical characteristics and tectonic-magmatic implications of the latest-Paleozoic volcanic rocks from Santanghu basin, eastern Xinjiang, northwest China. Acta Petrol. Sin. 22, 199–214.

Zhao, Z., Xiong, X., Wang, Q., Bai, Z., Qiao, Y., 2009. Late Paleozoic underplating in North Xinjiang: evidence from shoshonites and adakites. Gondwana Res. 16, 216–226.

Zhu, Y.F., Guo, X., Song, B., Zhang, L.F., Gu, L.B., 2009. Petrology, Sr–Nd–Hf isotopic geochemistry and zircon chronology of the Late Palaeozoic volcanic rocks in the southwestern Tianshan Mountains, Xinjiang, NW China. J. Geol. Soc. 166, 1085–1099.

Zindler, A., Hart, S., 1986. Chemical geodynamics. Ann. Rev. Earth Planet. Sci. 14, 493–571.